

Optically Enhanced Electric Field Sensing using Nitrogen-Vacancy Ensembles

M. Block,^{1,*} B. Kobrin,^{1,2,*} A. Jarmola,^{1,3,*} S. Hsieh,^{1,2} C. Zu,¹ N. L. Figueroa,^{4,5}
 V. M. Acosta,⁶ J. Minguzzi,⁷ J. R. Maze,⁴ D. Budker,^{1,5} and N. Y. Yao^{1,2}

¹Department of Physics, University of California, Berkeley, CA 94720, USA

²Materials Science Division, Lawrence Berkeley National Laboratory, Berkeley, California 94720, USA

³U.S. Army Research Laboratory, Adelphi, Maryland 20783, USA

⁴Institute of Physics, Ponticia Universidad Catolica de Chile, Santiago, Chile

⁵Helmholtz Institut Mainz, Johannes Gutenberg Universitat Mainz, 55128 Mainz, Germany

⁶Center for High Technology Materials and Department of Physics and Astronomy,
 University of New Mexico, Albuquerque, New Mexico 87131, USA

⁷Institute for Quantum Electronics, ETH Zurich, 8093 Zurich, Switzerland

(Dated: November 9, 2021)

Nitrogen-vacancy (NV) centers in diamond have shown promise as inherently localized electric-field sensors, capable of detecting individual charges with nanometer resolution. Working with NV ensembles, we demonstrate that a detailed understanding of the *internal* electric field environment enables enhanced sensitivity in the detection of *external* electric fields. We follow this logic along two complementary paths. First, using excitation tuned near the NV's zero-phonon line, we perform optically detected magnetic resonance (ODMR) spectroscopy at cryogenic temperatures in order to precisely measure the NV center's excited-state susceptibility to electric fields. In doing so, we demonstrate that the characteristically observed contrast inversion arises from an interplay between spin-selective optical pumping and the NV centers' local charge distribution. Second, motivated by this understanding, we propose and analyze a novel scheme for optically-enhanced electric-field sensing using NV ensembles; we estimate that our approach should enable order of magnitude improvements in the DC electric-field sensitivity.

Precision measurement of electric fields remains an outstanding challenge at the interface of fundamental and applied sciences [1–9]. Leading electric field sensors are often based upon nanoelectronic systems [10–16], electromechanical resonators [17, 18], or Rydberg-atom spectroscopy [19–24]. While such techniques offer exquisite sensitivities, their versatility can be limited by intensive engineering, calibration and operation requirements. More recently, quantum sensors based on solid-state defects have emerged as localized probes [25–42], offering nanoscale spatial resolution and the ability to operate under a wide variety of external conditions — e.g. ranging from cryogenic (~ 10 mK) to high temperatures (~ 600 K) [43, 44], from ambient to gigapascal pressures [45–48] and in the case of biological samples, directly *in-vivo* [49, 50].

Here, we focus on a particular defect, the negatively charged nitrogen-vacancy (NV) color center in diamond [50, 51]. As a spin defect with a long coherence time, which can be optically polarized and probed, the NV center has proven to be a versatile sensor, capable of measuring magnetic fields, temperature, stress, and, in the context of electric fields, detecting individual charges [25, 34, 52–54].

Despite this versatility, a key challenge for utilizing the NV center for electric field sensing is its relatively weak ground-state susceptibility [33, 55]. In principle, overcoming this challenge is possible through two distinct approaches: (i) leveraging the NV excited state, which exhibits a much larger coupling to electric fields, or (ii) utilizing high-density ensembles, which enhances the

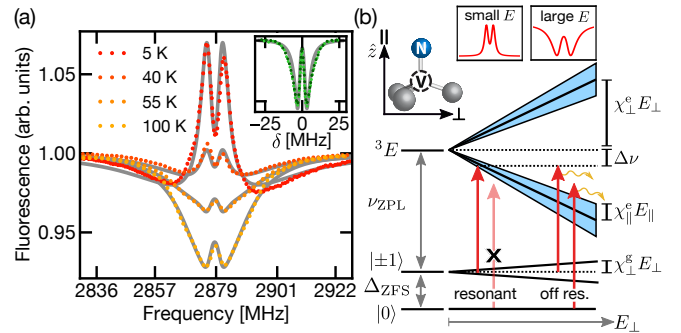


FIG. 1. (a) Resonant ODMR at varying temperatures with drive detuning $\Delta\nu \approx 156$ GHz below the ZPL. For $T \lesssim 45$ K, where the optical transition linewidth becomes smaller than Δ_{ZFS} [56], we observe the emergence of sharp positive-contrast peaks [57, 58]. Our numerical charge-based model (gray lines) quantitatively reproduces the experimental spectra. (Inset) The lineshape of the off-resonant ODMR as a function of δ , the microwave detuning from Δ_{ZFS} , at room temperature (dark green) and 5 K (light green) exhibits no temperature dependence. Resonant and off-resonant ODMR were performed at 0 magnetic field. Error bars are smaller than the marker size. (b) NV level structure in the presence of internal electric fields. The wavelength of the ZPL transition is approximately 637.2 nm, and resonant (off-resonant) ODMR is performed with an excitation wavelength of 636 – 639 nm (532 nm). The perpendicular field, $E_{\perp} = \sqrt{E_x^2 + E_y^2}$, splits the 3E manifold, while the parallel field, $E_{\parallel} = E_z$, shifts it (shaded blue region). Only perpendicular fields, which split $|m_s = \pm 1\rangle$ by $\chi_{\perp}^e E_{\perp}$, strongly affect the ground state [55]. Internal electric fields determine whether a given NV is: (i) *resonantly* driven (favored at small E), resulting in positive-contrast peaks, or (ii) *off-resonantly* driven (favored at large E), resulting in a negative contrast ODMR lineshape.

sensitivity as $\sim 1/\sqrt{N}$, the standard quantum limit [59].

Each of these approaches, however, faces its own obstacles. In the former case, single NV measurements of the excited-state electric-field susceptibilities are complicated by the photo-ionization of local charge traps [60–62]. In the latter case, higher densities exacerbate inhomogeneous broadening, which can ultimately overwhelm any statistical improvement in sensitivity.

In this Letter, we present two main results aimed at overcoming these obstacles. First, by leveraging an interplay between spin-selective optical pumping and internal electric fields [53, 63], we propose a method to extract the NV’s excited-state susceptibilities directly from ensemble optically detected magnetic resonance (ODMR) measurements. We implement this approach in a high-NV-density sample ($\rho_{\text{NV}} \sim 8$ ppm), extracting the transverse and longitudinal susceptibilities as $\chi_{\perp}^e = 1.4 \pm 0.1$ MHz/(V/cm) and $\chi_{\parallel}^e = 0.7 \pm 0.1$ MHz/(V/cm), respectively. Second, we propose a novel electric field sensing protocol that utilizes resonant optical excitation of NV ensembles. The protocol is optimal at low temperatures, where we expect a DC sensitivity, $\eta = 1.3 \pm 0.3$ mV/cm/ $\sqrt{\text{Hz}}$, representing a two order of magnitude improvement compared to the best known NV methods [33, 64]. Both of our results stem from the investigation of an unusual experimental feature — inverted-contrast ODMR peaks [Fig. 1(a)] — which arise in low-temperature spectroscopy performed with near-resonant excitation [57].

Inverted ODMR contrast.—The NV center hosts an electronic spin-triplet ground state, where, in the absence of perturbations, the $|m_s = \pm 1\rangle$ sublevels are degenerate and sit $\Delta_{\text{ZFS}} = 2.87$ GHz above the $|m_s = 0\rangle$ state [Fig. 1(b)]. In high-density NV ensembles, this degeneracy is lifted most strongly by the local charge environment which directly couples the $|m_s = \pm 1\rangle$ sublevels; this leads to typical ground-state ODMR spectra which exhibit a pair of heavy-tailed resonances centered around Δ_{ZFS} [inset, Fig. 1(a)] [53, 65].

Such ODMR spectra are usually obtained using continuous-wave *off-resonant* optical excitation, in which the NV center is initialized and read out with laser frequency detuned far above the zero-phonon line (ZPL), ν_{ZPL} [Fig. 1(b)]. Identical spectra are observed at both room temperature and cryogenic conditions [inset, Fig. 1(a)].

In contrast, continuous-wave ODMR spectra taken with an optical drive near resonance with the ZPL exhibit a marked temperature dependence characterized by two principal features [Fig. 1(a)]. Most prominently, for temperatures $\lesssim 45$ K, the resonances *invert*, becoming a pair of narrow, positive-contrast peaks [57]. The entire spectrum, however, does not invert: Rather, these sharp peaks sit inside a broad envelope of negative contrast which is relatively temperature independent.

To understand the coexistence of these features, one

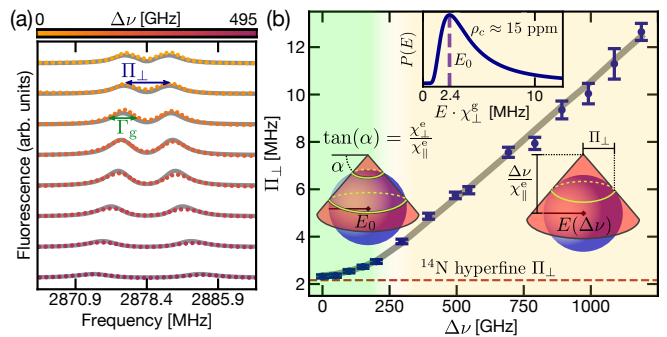


FIG. 2. (a) Resonant ODMR spectra as a function of $\Delta\nu$ taken under a 20 G magnetic field perpendicular to the NV axis. The positive-contrast peaks in the spectra are characterized by a splitting, Π_{\perp} , and a linewidth Γ_g . Gray lines correspond to our numerical model. Error bars are smaller than the marker size. (b) Π_{\perp} as a function of $\Delta\nu$. In the small detuning region (light green), the highest-probability electric-field sphere (blue) intersecting the resonant cone (red) is of radius E_0 [66]; in the large detuning region (light yellow), the radius of the highest-probability sphere that intersects the cone depends linearly on $\Delta\nu$. The red dashed line indicates the limit to Π_{\perp} imposed by the hyperfine interaction. By fitting our numerical model to this data (gray line), we extract the excited-state electric-field susceptibilities. (upper inset) The probability distribution $P(E)$ exhibits a peak at E_0 , which is determined by the charge density.

must consider the interplay between resonant optical pumping and the local charge environment. For resonant excitation, only one of the ground-state sublevels is driven to the excited state [Fig. 1(b)], leading to the accumulation of population in an optically dark state and, thus, a positive-contrast ODMR feature [57, 58]. However, the presence of local, internal electric fields perturbs the NV’s excited-state energy levels and modifies the optical resonance condition. In particular, perpendicular electric fields (relative to the NV axis) split both the ground-state and excited-state manifolds, leading to a distribution of resonant and off-resonant electric-field configurations [Fig. 1(b)] [67]. For small optical detunings, $\Delta\nu$, from the NV ZPL, *weak* electric fields are generally required to match the resonance condition; on the other hand, large electric fields favor the off-resonant mechanism. The NV’s ground-state splitting is also directly correlated with the strength of the electric field; this naturally explains why the positive-contrast feature is narrower and sits atop a broader negative-contrast background [Fig. 1(b)] [68].

Let us now turn our heuristic understanding into a quantitative microscopic model. In particular, we perform numerical simulations of both resonant and off-resonant ODMR spectra for a range of temperatures. The three ingredients of our numerics are as follows. First, in order to determine the internal electric field distribution, we randomly place an equal number of posi-

tive and negative elementary charges at overall density ρ_c [53, 58]. Second, motivated by experimental observations [69], we allow the relative amplitude of the resonant and off-resonant ODMR features to vary with temperature, corresponding to the temperature-dependent efficiency of the optical pumping mechanism [70]. Finally, we include additional broadening of the ODMR spectra arising from both intrinsic broadening (e.g. magnetic fields and strain) and power broadening [58].

We determine $\rho_c \approx 15 \pm 2$ ppm independently from the *off-resonant* ODMR spectra [inset, Fig. 1(a)]; this suggests an NV density of $\rho_{\text{NV}} \approx \rho_c/2 \approx 8$ ppm, which is consistent with prior density estimates for this sample [58, 71]. By optimizing the efficiency and broadening parameters [58], we obtain resonant ODMR spectra, which are in excellent agreement with the experimental data, as depicted in Fig. 1(a).

Extracting excited-state susceptibilities.—Interestingly, the observed positive-contrast ODMR peaks, despite being a feature of *ground-state* spectroscopy, contain information about the *excited-state* electric-field susceptibilities: χ_{\parallel}^e and χ_{\perp}^e . In particular, as shown in Fig. 2(a), we perform ODMR measurements of the inverted-contrast feature as a function of the optical detuning. By tracking how the splitting, Π_{\perp} , of the positive-contrast feature changes as a function of $\Delta\nu$, we fully determine the excited-state susceptibilities [Fig. 2(b)]. At its core, this ability to independently extract χ_{\parallel}^e and χ_{\perp}^e stems from the fact that Fig. 2(b) exhibits two distinct regimes: at small detunings, Π_{\perp} exhibits a suppressed dependence on $\Delta\nu$, while at large detunings, Π_{\perp} exhibits a linear dependence.

Let us now explain the origin of these two regimes. The splitting, Π_{\perp} , of the positive-contrast ODMR feature is controlled by: (i) the optical resonance condition and (ii) the distribution of electric fields. As shown in Fig. 1(b), the resonance condition is given by: $\chi_{\parallel}^e E_z + \chi_{\perp}^e \sqrt{E_x^2 + E_y^2} = \Delta\nu$ [72]. A slight rearrangement

$$E_z - \frac{\Delta\nu}{\chi_{\parallel}^e} = -\frac{\chi_{\perp}^e}{\chi_{\parallel}^e} \sqrt{E_x^2 + E_y^2} \quad (1)$$

immediately shows that this condition defines a “resonant cone” in electric field space with apex at $E_z = \Delta\nu/\chi_{\parallel}^e$ [Fig. 2(b)]. On the other hand, the electric-field distribution is spherically symmetric and thus, completely characterized by the probability distribution, $P(E)$, where $E = \sqrt{E_{\perp}^2 + E_{\parallel}^2}$ is the electric field magnitude. Crucially, the distribution $P(E)$ is peaked at a characteristic electric field, $E_0 \cdot \chi_{\perp}^e \approx 2.4$ MHz, set by ρ_c , and exhibits a heavy tail [inset, Fig. 2(b)].

For a given detuning, this provides a geometric interpretation for determining the electric field configurations most likely to match the resonance condition; in particular, these configurations are set by the highest-

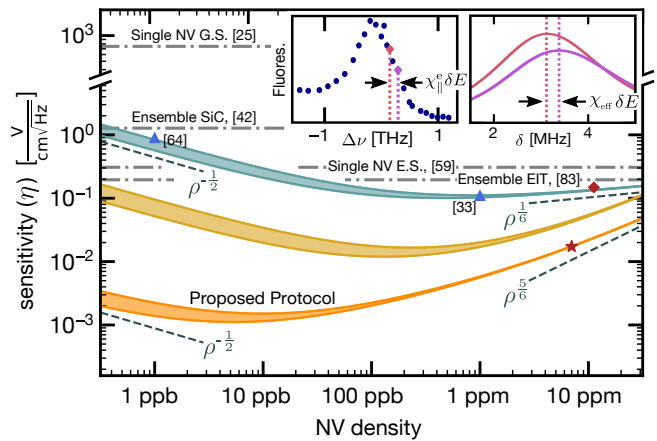


FIG. 3. Comparison of sensitivities for various solid-state defect electric field sensing methods. Light-blue region: estimated DC sensitivity using established NV ensemble electrometry techniques [33, 52, 64]. Additional demonstrations of NV electrometry include [73–75]. Orange (yellow) region: estimated sensitivity for our optically-enhanced protocol assuming an excited-state broadening of 10 GHz (100 GHz) and an illumination volume of 0.1 mm³ (10⁻³ mm³). Red star (diamond): estimated sensitivity for this sample at low temperature (for the optimal microwave-free variant of our protocol at 300 K). All sensitivities assume an intrinsic ODMR linewidth of 200 kHz. Dashed lines indicate asymptotic scaling of sensitivities. (left inset) Experimentally measured fluorescence as a function of $\Delta\nu$ [58]. An external field of strength δE results in a change in overall fluorescence. (right inset) Simulated peak shift in the resonant ODMR spectra for an external field of strength δE .

probability sphere that intersects the resonant cone [yellow circles in Fig. 2(b)]. At small detunings, the highest-probability sphere that intersects the resonant cone is always at radius E_0 , implying that $\Pi_{\perp} \sim E_0$ can only weakly depend on the detuning [66]. At large detunings, the sphere of radius E_0 no longer intersects the cone, and instead, the highest-probability intersecting sphere is simply the inscribed sphere [Fig. 2(b)]. The size of the inscribed sphere grows linearly with the detuning, and thus so does Π_{\perp} .

As a result of these two regimes, $\Pi_{\perp}(\Delta\nu)$ in Fig. 2(b) has both a slope and an elbow. By considering only the highest-probability intersecting sphere, one can analytically estimate χ_{\parallel}^e and χ_{\perp}^e directly from the location of the elbow and the value of the slope [58]. However, to be more precise, we determine Π_{\perp} from the full numerical model thus taking into account all resonant configurations [58]. We then find the susceptibilities that minimize the χ^2 error between the predicted and observed Π_{\perp} to extract: $\chi_{\perp}^e = 1.4 \pm 0.1$ MHz/(V/cm) and $\chi_{\parallel}^e = 0.7 \pm 0.1$ MHz/(V/cm) [gray line in Fig. 2(b)].

Our results are approximately two times larger than previous measurements via single NV Starks shifts [60–62]. We note that this discrepancy may be due to photo-

ionized charge traps, which have been shown to strongly affect single-NV measurements of excited-state susceptibilities [61, 62]. In contrast, our ensemble measurement of the susceptibilities does not rely on tuning an external voltage and thus is not directly sensitive to the nonlinear effects of charge traps [76].

Plugging the extracted susceptibilities into our resonant ODMR model fully reproduces the detuning-dependent experimental data [Fig. 2(a)]. In particular, the model quantitatively recovers two characteristic features of these spectra: a decrease in the overall fluorescence and an increase in the linewidth Γ_g , for increasing $\Delta\nu$ [58]. Physically, fluorescence declines with $\Delta\nu$ because the larger electric fields required for resonance are less likely. The dependence of Γ_g on $\Delta\nu$ is more subtle and is discussed in the supplementary material.

Optically enhanced electrometry.—Our understanding of the interplay between internal electric fields and resonant excitation suggests a novel protocol for DC electric field sensing using NV ensembles. The protocol is premised on the fact that an external electric field parallel to the NV axis induces an overall shift of the excited-state levels. In effect, this is equivalent to changing the optical detuning, which we have already observed has two primary consequences: (i) it alters the splitting of the inverted-contrast peaks (right inset, Fig. 3), and (ii) it changes the density of resonant configurations and therefore the overall fluorescence (left inset, Fig. 3).

To leverage these effects for electrometry, we propose the following protocol. First, apply a bias electric field parallel to one of the NV orientations to spectrally isolate its excited state [77]. Second, perform resonant ODMR with a fixed laser detuning below the peak of the ZPL, chosen such that positive-contrast peaks are clearly observed. Third, monitor the fluorescence at a fixed microwave drive frequency that maximizes the slope of the inner edge of one of the resonant peaks. Unlike typical NV electric field sensing methods, our protocol is designed to detect fields *parallel* to the NV axis [78].

The sensitivity of our protocol derives from the two aforementioned effects, which add constructively to change the fluorescence. In particular, the sensitivity owing to the peak shift alone is given by

$$\eta_{\Pi} = P_{\Pi} \frac{\Gamma_g}{\chi_{\text{eff}} C_{\text{MW}} C_r} \cdot \frac{1}{\sqrt{R}}, \quad (2)$$

where Γ_g is the linewidth of the positive-contrast peak, $P_{\Pi} \approx 0.77$ is a numerical factor associated with the lorentzian lineshape, $C_0 \approx 0.21$ is the inherent ODMR contrast, R is the total photon count rate, and $C_r \approx 0.55$ is the ratio of resonantly scattered photons to total photons [58, 79]. Note $\chi_{\text{eff}} \approx 0.41\chi_{\perp}^{\text{e}}$ is an effective susceptibility (right inset, Fig. 3) related to the slope of Π_{\perp} with respect to $\Delta\nu$ [Fig. 2(b)]. Similarly, the sensitivity arising from variations in the overall fluorescence is given

by

$$\eta_{\text{F}} = P_{\text{F}} \frac{\Gamma_e}{\chi_{\parallel}^{\text{e}} C_r} \cdot \frac{1}{\sqrt{R}}, \quad (3)$$

where Γ_e is the linewidth of the optical transition and $P_{\text{F}} \approx 0.39$ is a numerical lineshape factor determined from experimental data [58]. In combination, the overall electric field sensitivity of our method is given by: $1/\eta = 1/\eta_{\Pi} + 1/\eta_{\text{F}}$ [58].

For our current sample, one finds a sensitivity, $\eta = 17 \pm 4$ mV/cm/ $\sqrt{\text{Hz}}$, assuming an illumination volume of 0.1 mm^3 [64]. This represents a $5\times$ improvement over previous NV electrometry techniques (Fig. 3). The enhancement in sensitivity derives primarily from three factors: (i) a larger photon count rate due to resonant scattering, (ii) an improvement in contrast, and (iii) the ability to constructively combine the signal from peak-shifting and fluorescence variation, which provide comparable sensitivities individually.

The sensitivity of our protocol can be further improved by optimizing the NV density. Let us assume that the total charge density is twice the NV density (consistent with our sample). At low densities, η_{Π} and η_{F} are limited by the intrinsic broadening of resonant ODMR and the optical transition, respectively. By increasing density, both sensitivities improve according to the standard quantum limit, $\eta \propto 1/\sqrt{\rho_{\text{NV}}}$ — the usual motivation for performing ensemble sensing (Fig. 3). However, at sufficiently high densities, the broadening due to internal electric fields becomes larger than the intrinsic broadening and the sensitivity degrades (Fig. 3) [80]; intuitively, this occurs because the NV ensemble is primarily sensing electric fields within the diamond lattice rather than the external signal. In particular, one finds that the sensitivity degrades upon increasing density as $\eta \sim \rho_{\text{NV}}^{5/6}$ (Fig. 3) [58]. Conversely, the sensitivity improves rapidly upon decreasing density until one reaches the crossover density between the intrinsically-broadened and charge-broadened regimes.

Crucially, this crossover density is naturally different for η_{Π} and η_{F} . In particular, the non-charge-induced broadening of the *ground-state* ODMR linewidth is often limited to ~ 200 kHz by the ^{13}C nuclear spin bath (although isotopically purified samples can exhibit narrower linewidths) [81, 82]. This implies that η_{Π} is optimal at NV densities of ~ 30 ppb (Fig. 3). On the other hand, these same magnetic fields only weakly affect the excited state. Rather, the non-charge-induced broadening of the excited-state, whose origin is less well understood, has been empirically observed to be ~ 10 GHz [69, 83, 84]. This yields an optimal NV density for η_{F} of ~ 7 ppb.

Putting everything together, we obtain an optimal total sensitivity of $\eta = 1.3 \pm 0.3$ mV/cm/ $\sqrt{\text{Hz}}$ at an NV density ~ 10 ppb (Fig. 3). This represents an enhancement of two orders of magnitude compared to state-of-the-art NV methods.

A few remarks are in order. First, while our sensitivity estimates assume an optically-thin sample, comparable sensitivities may be achieved at larger optical depths by monitoring, for example, transmission amplitude instead of fluorescence [83]. Second, monitoring resonant fluorescence variation alone already provides a significant electric field sensitivity, yielding a straightforward microwave-free version of our protocol. Since this microwave-free protocol does not require one to track the positive-contrast ODMR feature, it can also be applied at room temperature [Fig. 1(a)]. Assuming a thermally broadened linewidth of ~ 2 THz at 300 K yields a sensitivity of ≈ 150 mV/cm/ $\sqrt{\text{Hz}}$ (Fig. 3); this is comparable to the best reported NV sensitivities at room temperature (albeit with a larger bias electric field [58]). Finally, our protocol may be extended to radiofrequency electrometry through Fourier analysis of the time-dependent fluorescence [85].

Our work opens the door to a number of intriguing future directions. First, in combination with recent work on diamond-surface-termination [34, 86], our protocol's enhanced sensitivities may help to mitigate the deleterious effects of surface screening, which currently limit the NV's ability to detect external electric fields [87–89]. Second, a more detailed study of the resonant ODMR lineshape as a function of detuning will provide insight into the microscopic distribution of charges within the diamond lattice [53, 58]; this in turn, can help in the development of novel strategies to suppress spectral diffusion [61, 90, 91].

Acknowledgments.—We gratefully acknowledge the insights of and discussions with A. Norambuena, T. Mitiga, P. Maletinsky, A. Jayich, and H. Zheng. We are especially grateful to K. M. Fu for sharing her raw data on the optical transition linewidth vs temperature. This work was supported as part of the Center for Novel Pathways to Quantum Coherence in Materials, an Energy Frontier Research Center funded by the U.S. Department of Energy, Office of Science, Basic Energy Sciences under Award No. DE-AC02-05CH11231. A.J. acknowledges support from the Army Research Laboratory under Cooperative Agreement no. W911NF-16-2-0008. S.H. acknowledges support from the National Science Foundation Graduate Research Fellowship under grant no. DGE-1752814. J.R.M. acknowledges support from Conicyt-Fondecyt grant 1880673 and AFOSR FA9550-18-1-0513. This work of D.B. was supported in part by the EU FET OPEN Flagship Project ASTERIQS.

* These authors contributed equally to this work.

- [1] K. M. Tyner, R. Kopelman, and M. A. Philbert, *Bio-physical journal* **93**, 1163 (2007).
 [2] K. J. Swartz, *Nature* **456**, 891 (2008).
 [3] C.-S. Lee, S. K. Kim, and M. Kim, *Sensors* **9**, 7111

- (2009).
 [4] L. Hall, G. Beart, E. Thomas, D. Simpson, L. McGuinness, J. Cole, J. Manton, R. Scholten, F. Jelezko, J. Wrachtrup, *et al.*, *Scientific reports* **2**, 401 (2012).
 [5] L. Jin, Z. Han, J. Platasa, J. R. Woollorton, L. B. Cohen, and V. A. Pieribone, *Neuron* **75**, 779 (2012).
 [6] R. S. Dhar, S. G. Razavipour, E. Dupont, C. Xu, S. Laframboise, Z. Wasilewski, Q. Hu, and D. Ban, *Scientific reports* **4**, 7183 (2014).
 [7] B. Le Feber, N. Rotenberg, D. M. Beggs, and L. Kuipers, *Nature Photonics* **8**, 43 (2014).
 [8] F. Huang, V. A. Tamma, Z. Mardy, J. Burdett, and H. K. Wickramasinghe, *Scientific reports* **5**, 10610 (2015).
 [9] D. Cadeddu, M. Munsch, N. Rossi, J.-M. Gérard, J. Claudon, R. J. Warburton, and M. Poggio, *Physical Review Applied* **8**, 031002 (2017).
 [10] O. Kolosov, A. Gruverman, J. Hatano, K. Takahashi, and H. Tokumoto, *Physical review letters* **74**, 4309 (1995).
 [11] J. Christman, H. Maiwa, S.-H. Kim, A. Kingon, and R. Nemanich, *MRS Online Proceedings Library Archive* **541** (1998).
 [12] R. G. Knobel and A. N. Cleland, *Nature* **424**, 291 (2003).
 [13] A. C. Johnson, J. R. Petta, C. M. Marcus, M. P. Hanson, and A. Gossard, *Physical Review B* **72**, 165308 (2005).
 [14] Y. Hu, H. O. H. Churchill, D. J. Reilly, J. Xiang, C. M. Lieber, and C. M. Marcus, *Nature Nanotechnology* **2**, 622 (2007).
 [15] G. J. Podd, S. J. Angus, D. A. Williams, and A. J. Ferguson, *Applied Physics Letters* **96**, 082104 (2010).
 [16] A. N. Vamivakas, Y. Zhao, S. Flt, A. Badolato, J. M. Taylor, and M. Atatire, *Physical Review Letters* **107**, 166802 (2011).
 [17] A. N. Cleland and M. L. Roukes, *Nature* **392**, 160 (1998).
 [18] J. S. Bunch, A. M. Van Der Zande, S. S. Verbridge, I. W. Frank, D. M. Tanenbaum, J. M. Parpia, H. G. Craighead, and P. L. McEuen, *Science* **315**, 490 (2007).
 [19] A. Facon, E.-K. Dietsche, D. Grosso, S. Haroche, J.-M. Raimond, M. Brune, and S. Gleyzes, *Nature* **535**, 262 (2016).
 [20] J. A. Sedlacek, A. Schwettmann, H. Kbler, R. Lw, T. Pfau, and J. P. Shaffer, *Nature Physics* **8**, 819 (2012).
 [21] H. Fan, S. Kumar, J. Sedlacek, H. Kbler, S. Karimkashi, and J. P. Shaffer, *Journal of Physics B: Atomic, Molecular and Optical Physics* **48**, 202001 (2015).
 [22] K.-Y. Liao, H.-T. Tu, S.-Z. Yang, C.-J. Chen, X.-H. Liu, J. Liang, X.-D. Zhang, H. Yan, and S.-L. Zhu, arXiv:2002.00855 [cond-mat, physics:physics, physics:quant-ph] (2020), arXiv: 2002.00855.
 [23] S. Kumar, H. Fan, H. Kbler, A. J. Jahangiri, and J. P. Shaffer, *Optics Express* **25**, 8625 (2017).
 [24] S. Kumar, H. Fan, H. Kbler, J. Sheng, and J. P. Shaffer, *Scientific Reports* **7**, 1 (2017).
 [25] F. Dolde, H. Fedder, M. W. Doherty, T. Nöbauer, F. Rempp, G. Balasubramanian, T. Wolf, F. Reinhard, L. C. Hollenberg, F. Jelezko, *et al.*, *Nature Physics* **7**, 459 (2011).
 [26] P. Klimov, A. Falk, B. Buckley, and D. Awschalom, *Physical Review Letters* **112**, 087601 (2014).
 [27] A. L. Falk, P. V. Klimov, B. B. Buckley, V. Ivády, I. A. Abrikosov, G. Calusine, W. F. Koehl, Á. Gali, and D. D. Awschalom, *Physical review letters* **112**, 187601 (2014).
 [28] Ö. Soykal, P. Dev, and S. E. Economou, *Physical Review*

- B **93**, 081207 (2016).
- [29] T. Iwasaki, W. Naruki, K. Tahara, T. Makino, H. Kato, M. Ogura, D. Takeuchi, S. Yamasaki, and M. Hatano, *ACS nano* **11**, 1238 (2017).
- [30] G. Wolfowicz, S. Whiteley, and D. Awschalom, *Proceedings of the National Academy of Sciences* **115**, 7879 (2018).
- [31] A. Ariyaratne, D. Bluvstein, B. A. Myers, and A. C. B. Jayich, *Nature communications* **9**, 2406 (2018).
- [32] I. Khivrich and S. Ilani, arXiv preprint arXiv:1908.08249 (2019).
- [33] J. Michl, J. Steiner, A. Denisenko, A. Blau, A. Zimmermann, K. Nakamura, H. Sumiya, S. Onoda, P. Neumann, J. Isoya, and J. Wrachtrup, *Nano Letters* **19**, 4904 (2019).
- [34] L. M. Oberg, M. O. de Vries, L. Hanlon, K. Strazdins, M. S. Barson, J. Wrachtrup, and M. W. Doherty, arXiv preprint arXiv:1912.09619 (2019).
- [35] Y. Zhou, J. Wang, X. Zhang, K. Li, J. Cai, and W. Gao, *Phys. Rev. Applied* **8**, 044015 (2017).
- [36] G. Wolfowicz, S. J. Whiteley, and D. D. Awschalom, *Proceedings of the National Academy of Sciences* **115**, 7879 (2018).
- [37] Z. Zhang, D. Schwanz, B. Narayanan, M. Kotiuga, J. A. Dura, M. Cherukara, H. Zhou, J. W. Freeland, J. Li, R. Sutarto, *et al.*, *Nature* **553**, 68 (2018).
- [38] D. Simin, V. A. Soltamov, A. V. Poshakinskiy, A. N. Anisimov, R. A. Babunts, D. O. Tolmachev, E. N. Mokhov, M. Trupke, S. A. Tarasenko, A. Sperlich, P. G. Baranov, V. Dyakonov, and G. V. Astakhov, *Phys. Rev. X* **6**, 031014 (2016).
- [39] C. J. Cochrane, J. Blacksberg, M. A. Anders, and P. M. Lenahan, *Scientific Reports* **6**, 37077 (2016).
- [40] C. P. Anderson, A. Bourassa, K. C. Miao, G. Wolfowicz, P. J. Mintun, A. L. Crook, H. Abe, J. Ul Hassan, N. T. Son, T. Ohshima, and D. D. Awschalom, *Science* **366**, 1225 (2019).
- [41] Q. Zhang, G. Hu, G. G. de Boo, M. Rancic, B. C. Johnson, J. C. McCallum, J. Du, M. J. Sellars, C. Yin, and S. Rogge, *Nano letters* **19**, 5025 (2019).
- [42] G. Wolfowicz, C. P. Anderson, S. J. Whiteley, and D. D. Awschalom, *Applied Physics Letters* **115**, 043105 (2019).
- [43] R. Amsüss, C. Koller, T. Nöbauer, S. Putz, S. Rotter, K. Sandner, S. Schneider, M. Schramböck, G. Steinhäuser, H. Ritsch, *et al.*, *Physical review letters* **107**, 060502 (2011).
- [44] D. Toyli, D. Christle, A. Alkauskas, B. Buckley, C. Van de Walle, and D. Awschalom, *Physical Review X* **2**, 031001 (2012).
- [45] M. W. Doherty, V. V. Struzhkin, D. A. Simpson, L. P. McGuinness, Y. Meng, A. Stacey, T. J. Karle, R. J. Hemley, N. B. Manson, L. C. Hollenberg, *et al.*, *Physical review letters* **112**, 047601 (2014).
- [46] M. Lesik, T. Plisson, L. Toraille, J. Renaud, F. Occelli, M. Schmidt, O. Salord, A. Delobbe, T. Debuisschert, L. Rondin, P. Loubeyre, and J.-F. Roch, *Science* **366**, 1359 (2019).
- [47] K. Y. Yip, K. O. Ho, K. Y. Yu, Y. Chen, W. Zhang, S. Kasahara, Y. Mizukami, T. Shibauchi, Y. Matsuda, S. K. Goh, and S. Yang, *Science* **366**, 1355 (2019).
- [48] S. Hsieh, P. Bhattacharyya, C. Zu, T. Mittiga, T. J. Smart, F. Machado, B. Kobrin, T. O. Hhn, N. Z. Rui, M. Kamrani, S. Chatterjee, S. Choi, M. Zaletel, V. V. Struzhkin, J. E. Moore, V. I. Levitas, R. Jeanloz, and N. Y. Yao, *Science* **366**, 1349 (2019).
- [49] G. Kucsko, P. C. Maurer, N. Y. Yao, M. Kubo, H. J. Noh, P. K. Lo, H. Park, and M. D. Lukin, *Nature* **500**, 54 (2013).
- [50] R. Schirhagl, K. Chang, M. Loretz, and C. L. Degen, *Annual review of physical chemistry* **65**, 83 (2014).
- [51] M. W. Doherty, N. B. Manson, P. Delaney, F. Jelezko, J. Wrachtrup, and L. C. Hollenberg, *Physics Reports* **528**, 1 (2013).
- [52] F. Dolde, M. W. Doherty, J. Michl, I. Jakobi, B. Naydenov, S. Pezzagna, J. Meijer, P. Neumann, F. Jelezko, N. B. Manson, *et al.*, *Physical review letters* **112**, 097603 (2014).
- [53] T. Mittiga, S. Hsieh, C. Zu, B. Kobrin, F. Machado, P. Bhattacharyya, N. Rui, A. Jarmola, S. Choi, D. Budker, *et al.*, *Physical review letters* **121**, 246402 (2018).
- [54] D. Bluvstein, Z. Zhang, and A. C. B. Jayich, *Physical review letters* **122**, 076101 (2019).
- [55] E. Van Oort and M. Glasbeek, *Chemical Physics Letters* **168**, 529 (1990).
- [56] K.-M. C. Fu, C. Santori, P. E. Barclay, L. J. Rogers, N. B. Manson, and R. G. Beausoleil, *Physical Review Letters* **103**, 256404 (2009).
- [57] R. Akhmedzhanov, L. Gushchin, N. Nizov, V. Nizov, D. Sobgayda, I. Zelensky, and P. Hemmer, *Physical Review A* **94**, 063859 (2016).
- [58] See Supplemental Material at [URL will be inserted by publisher] for additional information.
- [59] V. Giovannetti, S. Lloyd, and L. Maccone, *Science* **306**, 1330 (2004).
- [60] P. Tamarat, T. Gaebel, J. R. Rabeau, M. Khan, A. D. Greentree, H. Wilson, L. C. L. Hollenberg, S. Prawer, P. Hemmer, F. Jelezko, and J. Wrachtrup, *Physical Review Letters* **97**, 083002 (2006).
- [61] V. M. Acosta, C. Santori, A. Faraon, Z. Huang, K.-M. C. Fu, A. Stacey, D. A. Simpson, K. Ganesan, S. Tomljenovic-Hanic, A. D. Greentree, S. Prawer, and R. G. Beausoleil, *Physical Review Letters* **108**, 206401 (2012).
- [62] L. C. Bassett, F. J. Heremans, C. G. Yale, B. B. Buckley, and D. D. Awschalom, *Phys. Rev. Lett.* **107**, 266403 (2011).
- [63] J. Klbl, M. Kasperczyk, B. Brgler, A. Barfuss, and P. Maletinsky, *New Journal of Physics* **21**, 113039 (2019).
- [64] E. H. Chen, H. A. Clevenson, K. A. Johnson, L. M. Pham, D. R. Englund, P. R. Hemmer, and D. A. Braje, *Physical Review A* **95**, 053417 (2017).
- [65] Lattice strain effects have also been shown to lead to a split resonance in single NV centers [63]. However, typical strain fields result in *both* a shifting and splitting of the resonance. In ensembles, this naturally leads to a *single* broad peak instead of the observed split resonance [53]. In the case of electric fields, due to the large anisotropy between the transverse and longitudinal susceptibilities, local charges generically *split* the $|m_s = \pm 1\rangle$ sub-levels without significant *shifting*.
- [66] At small optical detunings, the highest-probability electric-field sphere (i.e. that of radius E_0) will actually intersect the resonant cone twice, leading the to the expectation of *two* resonant peaks. However, the width of $P(E)$ around E_0 broadens these features, resulting a single, slightly asymmetric peak.
- [67] We define a resonant configuration, at a given detuning, as a combination of transverse and longitudinal electric

- fields which cause the NV's ground to excited state transition to be resonantly driven by the optical excitation. Note that the resonance condition does not depend on the direction of the transverse component of the field in the plane perpendicular to the NV axis.
- [68] The positive contrast peaks arise from configurations with small electric fields, and hence small ground-state splittings, that are likely to be resonantly driven; the negative-contrast wings, meanwhile, arise from configurations with large electric fields, and hence large ground-state splittings, that are likely to be off-resonantly driven.
- [69] A. Batalov, V. Jacques, F. Kaiser, P. Siyushev, P. Neumann, L. J. Rogers, R. L. McMurtrie, N. B. Manson, F. Jelezko, and J. Wrachtrup, *Physical Review Letters* **102**, 195506 (2009).
- [70] V. M. Acosta, A. Jarmola, E. Bauch, and D. Budker, *Physical Review B* **82**, 201202 (2010).
- [71] V. M. Acosta, E. Bauch, M. P. Ledbetter, C. Santori, K.-M. C. Fu, P. E. Barclay, R. G. Beausoleil, H. Linget, J. F. Roch, F. Treussart, S. Chemerisov, W. Gawlik, and D. Budker, *Phys. Rev. B* **80**, 115202 (2009).
- [72] This resonance condition applies to the lower branch of the excited state. The corresponding resonance condition for the upper branch is given by $\chi_{\parallel}^{\circ} E_z - \chi_{\perp}^{\circ} \sqrt{E_x^2 + E_y^2} = \Delta\nu$. In Figure 2(b), we restrict our attention to the cone defined by the lower branch.
- [73] S. Sharma, C. Hovde, D. H. Beck, and F. Alghannam, arXiv preprint arXiv:1802.08767v1 (2018).
- [74] C. Hovde, S. Sharma, F. Alghannam, and D. H. Beck, in *Terahertz, RF, Millimeter, and Submillimeter-Wave Technology and Applications XI*, Vol. 10531, edited by L. P. Sadwick and T. Yang, International Society for Optics and Photonics (SPIE, 2018) pp. 103 – 110.
- [75] S. Sharma, C. Hovde, F. Alghannam, and D. H. Beck, in *Quantum Sensing and Nano Electronics and Photonics XIV*, Vol. 10111, edited by M. Razeghi, International Society for Optics and Photonics (SPIE, 2017) pp. 436 – 444.
- [76] We note, however, that photo-ionization effects could cause the charge density to depend on excitation wavelength [58, 61, 92].
- [77] In the supplementary material, we show that the necessary fields are similar in scale to those required in [64].
- [78] In the supplementary material, we show that the effects from perpendicular electric fields are suppressed to second order due to the random orientation of local fields and hence can be neglected in our discussion of sensitivity.
- [79] J. M. Taylor, P. Cappellaro, L. Childress, L. Jiang, D. Budker, P. R. Hemmer, A. Yacoby, R. Walsworth, and M. D. Lukin, *Nature Physics* **4**, 810 (2008).
- [80] Other perturbations to the NV level structure, such as strain and magnetic fields, can exacerbate ensemble broadening. For this discussion, we restrict attention to the ideal limit where there is minimal charge ($\rho_c = 2\rho_{NV}$) and there are no other significant density dependent sources of inhomogeneous broadening.
- [81] L. Pham, *Magnetic Field Sensing with Nitrogen-Vacancy Color Centers in Diamond*, Ph.D. thesis, Harvard University (2013).
- [82] G. Balasubramanian, P. Neumann, D. Twitchen, M. Markham, R. Kolesov, N. Mizuochi, J. Isoya, J. Achard, J. Beck, J. Tissler, V. Jacques, P. R. Hemmer, F. Jelezko, and J. Wrachtrup, *Nature Materials* **8**, 383 (2009).
- [83] V. M. Acosta, K. Jensen, C. Santori, D. Budker, and R. G. Beausoleil, *Phys. Rev. Lett.* **110**, 213605 (2013).
- [84] We emphasize that here we are referring to ensemble broadening; single NVs can exhibit nearly lifetime-limited excited state linewidths [60, 93–95].
- [85] C. S. Shin, C. E. Avalos, M. C. Butler, D. R. Trease, S. J. Seltzer, J. Peter Mustonen, D. J. Kennedy, V. M. Acosta, D. Budker, A. Pines, and V. S. Bajaj, *Journal of Applied Physics* **112**, 124519 (2012).
- [86] S. Cui and E. L. Hu, *Applied Physics Letters* **103**, 051603 (2013).
- [87] D. A. Broadway, N. Dontschuk, A. Tsai, S. E. Lillie, C. T.-K. Lew, J. C. McCallum, B. C. Johnson, M. W. Doherty, A. Stacey, L. C. L. Hollenberg, and J.-P. Tetienne, *Nature Electronics* **1**, 502 (2018), number: 9 Publisher: Nature Publishing Group.
- [88] A. Stacey, N. Dontschuk, J.-P. Chou, D. A. Broadway, A. K. Schenk, M. J. Sear, J.-P. Tetienne, A. Hoffman, S. Praver, C. I. Pakes, A. Tadich, N. P. d. Leon, A. Gali, and L. C. L. Hollenberg, *Advanced Materials Interfaces* **6**, 1801449 (2019).
- [89] M. Mertens, M. Mohr, K. Brhne, H. J. Fecht, M. ojkowski, W. wiskowski, and W. ojkowski, *Applied Surface Science* **390**, 526 (2016).
- [90] J. Wolters, N. Sadzak, A. W. Schell, T. Schröder, and O. Benson, *Physical review letters* **110**, 027401 (2013).
- [91] Y. Chu, N. P. de Leon, B. J. Shields, B. Hausmann, R. Evans, E. Togan, M. J. Burek, M. Markham, A. Stacey, A. S. Zibrov, *et al.*, *Nano letters* **14**, 1982 (2014).
- [92] N. B. Manson, M. Hedges, M. S. J. Barson, R. Ahlefeldt, M. W. Doherty, H. Abe, T. Ohshima, and M. J. Sellars, *New Journal of Physics* **20**, 113037 (2018).
- [93] Viktoria Yurgens, Josh A. Zuber, Sigurd Flagan, Marta De Luca, Brendan Shields, Tomasz Jakubczyk, Ilaria Zardo, Patrick Maletinsky, and Richard J. Warburton (2020).
- [94] S. B. van Dam, M. Walsh, M. J. Degen, E. Bersin, S. L. Mouradian, A. Galiullin, M. Ruf, M. IJspeert, T. H. Taminiau, R. Hanson, and D. R. Englund, *Physical Review B* **99**, 161203 (2019), publisher: American Physical Society.
- [95] Y. Chu, N. de Leon, B. Shields, B. Hausmann, R. Evans, E. Togan, M. J. Burek, M. Markham, A. Stacey, A. Zibrov, A. Yacoby, D. Twitchen, M. Loncar, H. Park, P. Maletinsky, and M. Lukin, *Nano Letters* **14**, 1982 (2014), publisher: American Chemical Society.

Supplementary Material: Optically Enhanced Electric Field Sensing using Nitrogen-Vacancy Ensembles

M. Block,* B. Kobrin,* A. Jarmola,* S. Hsieh, C. Zu, N. L. Figueroa,
 V. M. Acosta, J. Minguzzi, J. R. Maze, D. Budker, and N. Y. Yao
 (Dated: November 9, 2021)

CONTENTS

I. Experimental methods	1
II. Inverted contrast mechanism	2
III. Microscopic model	3
A. Electric field distribution	3
B. Resonance condition	5
C. Resonant ODMR spectra	5
IV. Extracting susceptibilities	7
V. Fitting temperature dependent spectra	9
VI. Sensitivity estimates	10
A. Parameter calibration	11
B. Scaling with density	13
C. Insensitivity to perpendicular fields	14
VII. Theoretical estimates of susceptibilities	14
A. Excited state	14
B. Ground state	15
References	17

I. EXPERIMENTAL METHODS

The experimental apparatus is illustrated in Fig. S1(a). A resonant (636-639 nm, 0.2 mW) or off-resonant (532 nm, ~ 1 mW) laser light is focused with a 0.5 numerical-aperture, 8 mm focal length aspheric lens onto the surface of a (111)-cut diamond housed in a continuous-flow cryostat (Janis ST-500). Fluorescence was collected using the same lens, spectrally filtered (within 650 – 800 nm), and detected with a Si photodiode. Microwaves were delivered by a 75 μm diameter copper wire running across the surface of the diamond. The temperature was measured with a diode located at the base of the cryostat's sample holder.

The diamond used in this work, labeled S2 in [2], was grown under high-pressure-high-temperature conditions (HPHT) and initially contained ~ 100 ppm of substitutional nitrogen. It was then irradiated with 3 MeV electrons at a dose of 10^{19} cm^{-2} in order to produce a uniform distribution of vacancies, and subsequently annealed at 1050 $^{\circ}\text{C}$ for two hours in order to facilitate the formation of NV centers by mobilizing the vacancies. After this treatment, the sample contains ~ 16 ppm of NV^- and ~ 50 ppm of unconverted substitutional nitrogen or NV^0 based on ZPL intensity measurements [2]. We note that this estimate of the NV density is $\sim 2\times$ larger than that of the charge-based model (see Section IV).

* These authors contributed equally to this work.

Parameter	Description	Value
$\Delta\nu$	Optical detuning from the zero-phonon-line (ZPL)	[-THz,THz]
Δ_{ZFS}	Ground-state zero-field splitting	2.879 GHz
Π_{\perp}	Splitting of positive-contrast ODMR feature	See Fig. 2(a)
$\chi_{\perp}^{\text{g}}, \chi_{\parallel}^{\text{g}}$	Ground-state electric-field susceptibilities	$\{17 \pm 2.5, 0.35 \pm 0.02\}$ Hz/(V/cm)[1]
χ_{eff}	Effective susceptibility of resonant ODMR	6.97 Hz/(V/cm); See Table III
$\chi_{\perp}^{\text{e}}, \chi_{\parallel}^{\text{e}}$	Excited-state electric-field susceptibilities	$\{1.4 \pm 0.2, 0.7 \pm 0.2\}$ MHz/(V/cm)
ρ_c (ρ_{NV})	Total charge density (density of NV centers)	15 ± 2 (8 ± 1) ppm
E_0	Strength of highest-probability electric field	$2.4 \text{ MHz}/\chi_{\perp}^{\text{g}}$
Γ_{g}	Linewidth of ground-state ODMR spectrum	See Table III and Fig. S6
Γ_{e}	Linewidth of optical transition between the 3A_2 ground state and the ensemble-broadened 3E excited state	See Table III
κ_{IH}	Ground-state inhomogeneous broadening due to magnetic fields (i.e. $1/(\pi T_2^*)$ under applied magnetic field)	1.7 ± 0.3 MHz
κ_{H}	Ground-state homogeneous broadening, e.g. due to microwave power broadening	1.0 ± 0.2 MHz
η_{II} (η_{F})	Electric field sensitivity owing to peak shift (overall fluorescence)	See Table III
R	Total photon count rate	See Table III
C_{r}	Ratio of resonantly scattered photons to total photons	See Table III
C_0	Maximum continuous-wave contrast of the resonant ODMR peaks	0.21

TABLE I. Summary of common parameters and their associated values.

II. INVERTED CONTRAST MECHANISM

Here, we elaborate on the physical origin of the positive-contrast peaks observed in resonant optically detected magnetic resonance (ODMR). Our explanation is consistent with that of Ref. [3], with the exception that their work attributed the inhomogeneous broadening of the optical transition primarily to strain rather than to internal electric fields.

To begin, let us recall that in the case of *off-resonant* optical excitation, the $|m_s = \pm 1\rangle$ states fluoresce less brightly than the $|m_s = 0\rangle$ state. Moreover, in the absence of microwave excitation, the NV population accumulates in the $|m_s = 0\rangle$ state, owing to the spin-selective branching ratio of the singlet-decay channel. Applying resonant microwave excitation thus drives the population from the (brighter) $|m_s = 0\rangle$ state to the (dimmer) $|m_s = \pm 1\rangle$ states. This leads to the typically observed negative-contrast ODMR feature.

On the other hand, in the case of *resonant* excitation, one of the sublevels may be driven resonantly to the excited state manifold, while the other sublevel does not satisfy the resonance condition and remains dark. Then, the same singlet-decay channel leads to the accumulation of population in the effective dark state [4]. Under microwave excitation, population is restored to the bright state, leading to an increased fluorescence and, hence, a positive-contrast ODMR feature [Fig. S1(c)].

We note that this mechanism does not depend on which of the sublevels ($|m_s = 0\rangle$ or $|m_s = \pm 1\rangle$) acts as the bright state, since there exists a finite matrix element between each of the ground-state sublevels

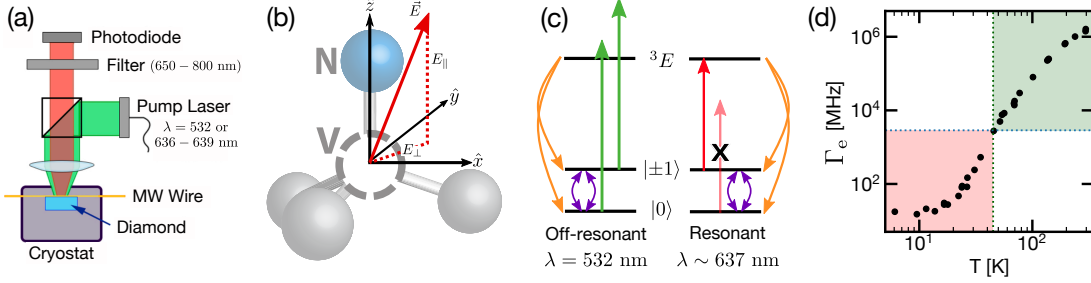


FIG. S1. (a) Experimental setup. Both green and red lasers can be used for NV excitation. (b) Schematic of the nitrogen-vacancy (NV) center and definition of coordinates used throughout this work. (c) Off-resonant (left) and resonant (right) excitation schemes. Under resonant excitation, an effective dark state ($|0\rangle$ above) results in *increased* fluorescence on microwave resonance. (d) Optical transition linewidth (Γ_e) as a function of temperature. Data reproduced from [5]. In the green-shaded region, $\Gamma_e > \Delta_{\text{ZFS}}$ and no inverted contrast is observed; in the red-shaded region $\Gamma_e < \Delta_{\text{ZFS}}$ and resonant excitation yields inverted contrast ODMR.

and the excited state; indeed, an ensemble average would include signal from each of these transitions. The resonant mechanism does, however, depend on temperature: it can only occur if the thermally-broadened optical transition linewidth is smaller than Δ_{ZFS} , a situation that arises for $T \lesssim 45$ K [Fig. S1(d)]. Above this temperature, one expects the positive-contrast feature to disappear, a prediction that is confirmed experimentally [Fig. 1(a)].

As shown in Fig. S2, the positive-contrast feature also exhibits a strong dependence on the optical detuning. For drives below ZPL, the positive-contrast peaks are clearly visible and are described quantitatively by our microscopic model (see Section III); in contrast, for drives above ZPL, the positive-contrast peaks disappear with increasing detuning (Fig. S2). We ascribe this disappearance to the fact that the resonance condition is most likely to be met by the *upper branch* of the 3E manifold at these detunings, but this branch is itself within the phonon-sideband of the lower branch. Hence, excited states of the upper branch will have shorter lifetimes than their lower branch counterparts, possibly rendering the linewidth of the associated optical transitions too large for the positive-contrast feature to emerge.

Lastly, we emphasize that the contrast of the positive-contrast features can exceed that of off-resonant ODMR features. In particular, the contrast of off-resonant ensemble ODMR is limited to a few percent by the branching ratio and the relative fluorescence of the spin sublevels. While the limiting factors for the contrast of resonant ODMR are not as well understood, empirically its value has been observed to be between 30% and 50% [3]. In principle, the contrast may improved further with sample optimization. In our sensitivity estimates, we assume a contrast of 21%, which is the value extracted from our experimental data [Fig. S7(c)].

III. MICROSCOPIC MODEL

A. Electric field distribution

Our microscopic model for resonant ODMR is based on the assumption that internal electric fields are primarily responsible for determining the optical resonance condition. Moreover, we assume these fields are produced by an ensemble of randomly placed, localized charges with an overall density, ρ_c [6]^[a]. This electric field distribution can be numerically sampled via Monte Carlo techniques by placing many charges at random and adding their electric fields. However, to improve the efficiency of our analysis, we choose to approximate this distribution with an analytic expression. In particular, we find that the desired electric field distribution owing to an *ensemble* of random charges at density ρ_c is in good agreement with a simpler distribution arising from the *single* nearest charge in an ensemble with an effective density ρ_{eff} [Fig. S3(a)].

^[a] The sign of the charges does not affect the overall electric field distribution, provided that the positions of the charges are independently distributed; for instance, the electric field produced by a positive charge is equivalent to that produced by a negative charge whose position is inverted with respect to the NV, which has equal probability. Additional details on the physical origin of the charges are provided at the end of this section.

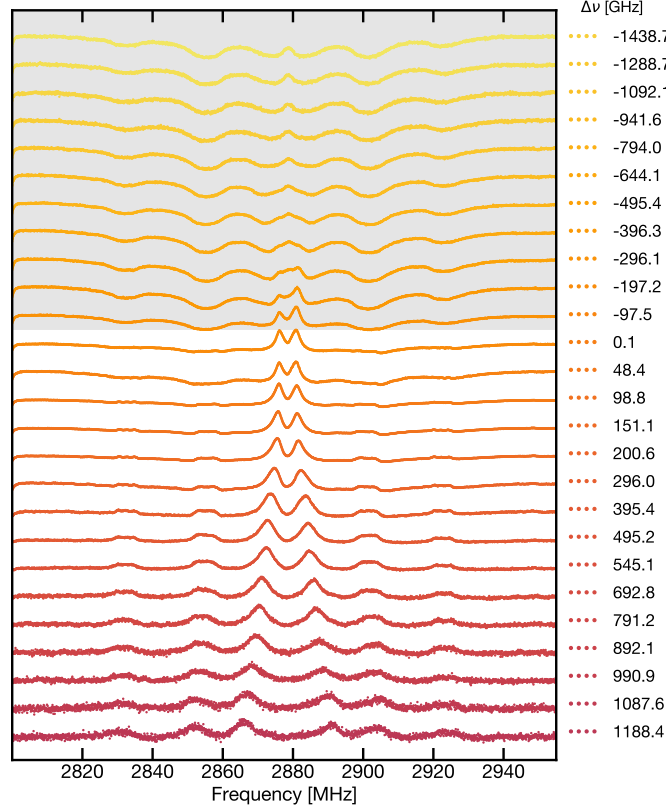


FIG. S2. Resonant ODMR spectra at varying optical detuning; shaded background corresponds to detunings above ZPL, while white background corresponds to detunings below ZPL. The spectra were taken with a 20 G magnetic field applied in the plane of the (111)-cut diamond (i.e. perpendicular to one NV axis). Smaller peaks, split $\gtrsim 20$ MHz from the center frequency, correspond to microwave resonance with other NV groups. Other presentations of these spectra restrict focus to the central group at detunings below ZPL.

Both distributions are spherically symmetric (i.e. the orientation of \vec{E} is distributed uniformly over the unit sphere), so it is sufficient to define the probability density for the electric field magnitude, $P(E)$. For the single charge model, the electric field magnitude is determined by the distance of the *nearest* charge within an ensemble of randomly placed charges. This probability density is given by

$$P_r(\tilde{r}) d\tilde{r} = 4\pi\tilde{r}^2 \exp\left\{-\frac{4}{3}\pi\tilde{r}^3\right\} d\tilde{r} \quad (1)$$

in normalized units $\tilde{r} = r\rho_{\text{eff}}^{1/3}$. Converting to electric field, i.e. $\tilde{E} = 1/\tilde{r}^2$, yields the electric field distribution

$$P_E(\tilde{E}) d\tilde{E} = P_r\left(\frac{1}{\tilde{E}^{1/2}}\right) \frac{1}{2\tilde{E}^{3/2}} d\tilde{E} \quad (2)$$

$$= \frac{4\pi}{\tilde{E}^{5/2}} \exp\left\{-\frac{4\pi}{3\tilde{E}^{3/2}}\right\} d\tilde{E} \quad (3)$$

in normalized units $\tilde{E} = E/E_{\text{ref}}$, where $E_{\text{ref}} = \rho^{2/3}/(4\pi\epsilon_0\epsilon_r)$, ϵ_0 is the vacuum permittivity, and ϵ_r is the relative permittivity of diamond, which we take to be 5.7 [7].

To check the validity of this distribution and determine ρ_{eff} , we compare $P(E) \equiv P_E(E)$ to Monte Carlo simulations of a full charge ensemble [Fig. S3(a)]. The two distributions exhibit good agreement for $\rho_{\text{eff}} \approx$

$0.5\rho_c$; in particular, both are peaked at $E_0 \propto \rho_c^{2/3}$ and exhibit a slowly decaying tail for $E > E_0$ [b].

Let us now briefly discuss the physical origin of the local charge environment. We expect these charges to consist primarily of other (negatively charged) NV centers and of positively charged defects. Motivated by charge neutrality, we postulate that these two types of charges are present with the same density, leading to the expectation that $\rho_c \approx 2\rho_{\text{NV}}$. For samples across a wide range of densities, this prediction agrees with expected NV densities based on sample specification [6]. However, we anticipate that corrections to our simple picture may arise from other charged defects not involved with the electron donor process (e.g. charged vacancy centers), or the possibility that the charge donors are localized near their associated NV centers (leading to enhanced electric fields). Either effect would increase the effective charge density; thus, it is more appropriate to consider the lower bound, $\rho_c \geq 2\rho_{\text{NV}}$. For our sensitivity estimates, we neglect these potential complications and consider the optimal scenario where $\rho_c \approx 2\rho_{\text{NV}}$.

B. Resonance condition

To determine the resonance condition, we model the ${}^3\text{E}$ excited state as two branches (upper and lower) of states, whose energies relative to ν_{ZPL} are given by [8, 9]

$$\Delta\nu_{\text{U,L}}(\vec{E}) = \chi_{\parallel}^e E_{\parallel} \mp \chi_{\perp}^e E_{\perp} \quad (4)$$

with E_{\parallel} , E_{\perp} defined in Fig. S1(b) (note that in our notation positive detuning is *below* the ZPL). This simplified level structure ignores the spin-orbit coupling, which generally splits each branch into three individual states. However, this simplification is justified when the splitting due to transverse electric fields exceeds ~ 10 GHz, which we find corresponds to charge densities greater than ~ 10 ppb based on the extracted susceptibilities and microscopic charge model.

We then consider a given NV to be resonantly driven by a laser with detuning $\Delta\nu$ if

$$\left| \Delta\nu_{\text{U}}(\vec{E}) - \Delta\nu \right| \leq \gamma_e/2 \quad \text{or} \quad \left| \Delta\nu_{\text{L}}(\vec{E}) - \Delta\nu \right| \leq \gamma_e/2, \quad (5)$$

where γ_e is the single-NV linewidth of the optical transition (including laser power broadening), and is henceforth assumed to be less than $\Delta\nu_{\text{ZFS}}$ [Fig. S1(d)]. While the precise value of γ_e does not affect the ODMR lineshapes, since it is generally much smaller than the optical transition ensemble linewidth Γ_e , it does determine the absolute fraction of NVs that are on or off resonance. This allows us to compare the observed resonant fluorescence to the predicted fluorescence from single NV measurements, as discussed below [see (16)].

C. Resonant ODMR spectra

We now state our model for resonant ODMR spectra. This consists of two related tasks: (i) determining the ODMR lineshape, taking into account both resonant and off-resonant configurations, and (ii) calculating the overall background fluorescence.

ODMR lineshape: We begin by defining a primitive ground-state lineshape for a single electric field configuration. This lineshape, denoted $\Lambda(\omega; E_{\perp})$, is parameterized by the perpendicular electric field E_{\perp} , which determines the splitting between the $|m_s = \pm 1\rangle$ sublevels. In addition, it depends on an inhomogeneous broadening parameter κ_{IH} , arising from local magnetic fields, and a homogeneous broadening parameter κ_{H} , due to microwave power broadening and strain. The difference between the two forms of broadening is that inhomogeneous broadening adds in quadrature with the electric field splitting, while homogeneous broadening is treated as an overall convolution. More specifically, we model both forms of broadening as a Lorentzian distribution, where κ is the full-width-half-maximum (FWHM). We further take into account the effective

[b] In fact, neither the analytic nor the Monte Carlo model agrees precisely with the heavy tails seen in the off-resonant ODMR spectra [Fig. 1(a), inset]. Since large fields are determined by nearby charges, this indicates that a model of randomly placed charges does not fully capture the short-range physics in the vicinity of the NV centers. These large-field discrepancies likely lead to errors in our estimation of the linewidth and contrast of the positive-contrast feature as function of detuning, but have negligible impact on the splitting and hence our susceptibility analysis.

magnetic field, $\mu_B g_e B_I \in \{0, \pm 2.16 \text{ MHz}\}$ owing to the three distinct ^{14}N nuclear states, i.e. $m_I = 0, \pm 1$. Altogether, the explicit form for $\Lambda(\omega; E_\perp)$ is given by

$$\Lambda_{\text{IH}}(\omega; E_\perp) = \begin{cases} 0 & |\omega| \leq \chi_\perp^g E_\perp \\ \sum_{B_I} \frac{\frac{\kappa_{\text{IH}}}{2} |\omega|}{\pi \sqrt{\omega^2 - (\chi_\perp^g E_\perp)^2} \left((|\mu_B g_e B_I| - \sqrt{\omega^2 - (\chi_\perp^g E_\perp)^2})^2 + (\frac{\kappa_{\text{IH}}}{2})^2 \right)} & |\omega| > \chi_\perp^g E_\perp \end{cases} \quad (6)$$

$$\Lambda(\omega; E_\perp) = \int d\omega' \Lambda_{\text{IH}}(\omega; E_\perp) \frac{\frac{\kappa_{\text{H}}}{2}}{\pi \left[(\omega - \omega')^2 + (\frac{\kappa_{\text{H}}}{2})^2 \right]}, \quad (7)$$

where $\Lambda_{\text{IH}}(\omega; E_\perp)$ is the lineshape with inhomogeneous broadening alone.

To determine the spectrum due to only resonant configurations, we integrate over primitive lineshapes that match the resonance condition:

$$S_{\text{R}}(\omega; \Delta\nu) = \int dE P(E) \int \sin(\theta) d\theta \Lambda_{\text{R}}(\omega; E_\perp) D_{\text{R}}(\vec{E}, \Delta\nu), \quad (8)$$

where $\vec{E} = (E_\perp, E_\parallel) = (E \sin \theta, E \cos \theta)$. $D_{\text{R}}(\vec{E}, \Delta\nu)$ is 1 on resonance and 0 otherwise:

$$D_{\text{R}}(\vec{E}, \Delta\nu) = [\Theta(\gamma_e/2 - |\delta_{\text{U}}|/2) + \Theta(\gamma_e/2 - |\delta_{\text{L}}|/2)] \quad (9)$$

$$\delta_{\text{U,L}} = \Delta\nu - \Delta\nu_{\text{U,L}}(\vec{E}), \quad (10)$$

where Θ is the Heaviside step function. Using the analytic expression for $P(E)$, $S_{\text{R}}(\omega; \Delta\nu)$ can be efficiently evaluated with numerical integration.

Similarly, the spectrum due to off-resonant configurations is given by:

$$S_{\text{OR}}(\omega; \Delta\nu) = \int dE P(E) \int \sin(\theta) d\theta \Lambda_{\text{R}}(\omega; \sin(\theta)E) D_{\text{OR}}(\vec{E}, \Delta\nu) \quad (11)$$

$$D_{\text{OR}}(\vec{E}, \Delta\nu) = [\Theta(\delta_{\text{U}} - \gamma_e/2) + \Theta(\delta_{\text{L}} - \gamma_e/2)]. \quad (12)$$

We note that $D_{\text{OR}}(\vec{E}, \Delta\nu)$ can take three values: 0 if the optical drive is below both branches, 1 if it is between the two branches, and 2 if it is above both branches; this is because the phonon sidebands of each excited state branch can contribute to the off-resonant cross-section.

Adding the two cases together with a relative contrast factor, ϵ_C , yields the full spectrum:

$$S_{\text{tot}}(\omega; \Delta\nu) = \epsilon_C S_{\text{R}}(\omega; \Delta\nu) - S_{\text{OR}}(\omega; \Delta\nu). \quad (13)$$

The sign difference captures the fact that off-resonant configurations are associated with negative-contrast features, while resonant configurations are associated with positive-contrast features. Additionally, the resonant and off-resonant contributions may have different linewidth parameters (see Section V). The relative contrast factor ϵ_C is related to both the enhanced cross-section of the resonant scattering (denoted ϵ_{R} below) and the intrinsic contrast difference of (single NV) resonant and off-resonant ODMR spectra; we find that this parameter is relevant for the temperature-dependent fits but not for our susceptibility extraction. Finally, we emphasize our model depends on the excited state electric field susceptibilities of the NV center through $\delta_{\text{U,L}}$.

Fluorescence: The total fluorescence is determined by the fraction of resonant and off-resonant configurations. These fractions are given by

$$F_{\text{R}}(\Delta\nu) = \frac{1}{\mathcal{N}} \int dE P(E) \int \sin(\theta) d\theta D_{\text{R}}(\vec{E}, \Delta\nu) \quad (14)$$

$$F_{\text{OR}}(\Delta\nu) = \frac{1}{\mathcal{N}} \int dE P(E) \int \sin(\theta) d\theta D_{\text{OR}}(\vec{E}, \Delta\nu), \quad (15)$$

where \mathcal{N} is the total number of configurations. $F_{\text{OR}}(\Delta\nu)$ and $F_{\text{R}}(\Delta\nu)$ are shown for various charge densities in Fig. S3(b) and S3(c), respectively. The total fluorescence is a weighted sum of these two contributions:

$$R(\Delta\nu) \propto \epsilon_{\text{R}} F_{\text{R}}(\Delta\nu) + F_{\text{OR}}(\Delta\nu), \quad (16)$$

where ϵ_{R} is the enhancement factor of the resonant mechanism. From single NV experiments, we estimate $\epsilon_{\text{R}} \approx 10^5$ [10]. Up to overall rescaling, we can then calculate the predicted fluorescence as a function of detuning; this exhibits good agreement with the background fluorescence as shown in Figure S7(b).

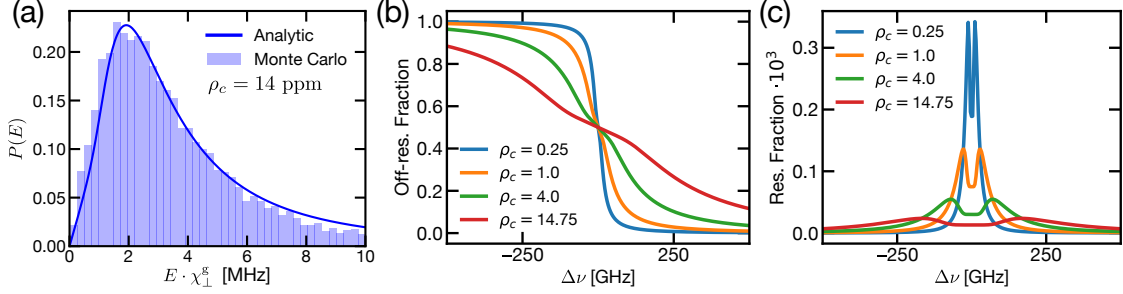


FIG. S3. (a) Comparison of analytic and Monte Carlo models of $P(E)$. The two methods agree in the vicinity of E_0 provided the analytic model is evaluated with a rescaled effective charge, $\rho_{\text{eff}} \approx 2\rho_c$. (b) Fraction of off-resonant configurations as a function of $\Delta\nu$. (c) Fraction of resonant configurations as a function of $\Delta\nu$. The density of resonant configurations is peaked sharply around $\Delta\nu = 0$, with a slope and maximum that scale as $\rho_c^{-2/3}$.

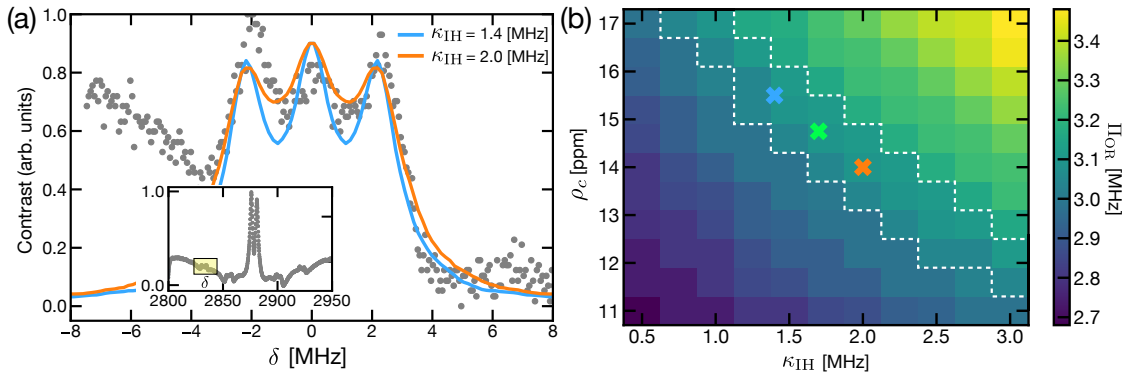


FIG. S4. (a) Resonant ODMR spectrum with optical drive detuned 190 GHz below ZPL and magnetic field applied in the plane of the (111)-cut diamond. We focus on the lineshape of an NV sub-ensemble experiencing a large magnetic field projection along its axis. Solid blue and orange traces are triple-Lorentzian lineshapes with widths 1.4 MHz and 2.0 MHz respectively; these are used to constrain the inhomogeneous broadening, κ_{IH} . (inset) The full resonant ODMR spectrum. The peaks shown in the main panel are located in highlighted box. (b) Predicted off-resonant ODMR splitting as a function of charge density ρ_c and κ_{IH} . The white-dashed contour indicates the region for which the predicted splitting value is consistent with the room-temperature spectrum [Fig. 1(a), inset]. This region, coupled with the extracted range for κ_{IH} , is used to constrain the acceptable values of ρ_c . We extract susceptibilities for three pairs $(\rho_c, \kappa_{\text{IH}})$, indicated by the colored x-markers, spanning this range.

IV. EXTRACTING SUSCEPTIBILITIES

As discussed in the main text, we extract the excited-state electric field susceptibilities by fitting our model to the measured splitting of the positive-contrast peak, Π_{\perp} , as a function optical detuning, $\Delta\nu$. Here, we provide additional details on this procedure, including error estimation and the determination of model parameters, i.e. the charge density and broadening parameters.

To begin, we determine Π_{\perp} as a function of detuning from the experimentally measured ODMR spectra [Fig. 2(a)]. In particular, we identify the frequency of the local maximum, ω_{\pm} , associated with each positive-contrast peak and compute $\Pi_{\perp} = \frac{1}{2}(\omega_{+} - \omega_{-})$. The uncertainty on these estimates arises from shot noise in the resonant ODMR spectra, which causes the frequency of maximum fluorescence to vary between successive measurements. To determine this uncertainty, we perform a Monte Carlo simulation of Lorentzian lineshapes with Gaussian noise, whose strength is determined from the experimental data, and sample the frequency of local maximum; this yields the error bars shown in Fig. 2(b) and S5(a).

We next determine the three parameters required in our resonant ODMR model (see Section III) other than the susceptibilities through the following independent calibration steps:

1. Inhomogeneous broadening, κ_{IH} : We measure the resonant ODMR spectrum of an NV sub-ensemble with a significant magnetic field projection along its axis [Fig S4(a)]. Since this magnetic field suppresses

electric field noise, the dominant source of remaining noise is due to inhomogeneous magnetic fields. Fitting this spectrum to three Lorentzians yields an inhomogeneous linewidth $\kappa_{\text{IH}} = 1.7 \pm 0.3$ MHz [Fig. S4(a)].

2. Charge density, ρ_c : We measure a room-temperature, off-resonant ODMR spectrum without a bias magnetic field. The characteristic splitting observed in this spectrum is fit to our model of randomly placed charges, leading to a charge-density estimate of $\rho_c = 15 \pm 2$ ppm.
3. Homogeneous broadening, κ_{H} : We perform a Lorentzian fit to the positive-contrast features of an ODMR spectrum measured with optical excitation near the zero-phonon-line ($\Delta\nu \lesssim 1$ GHz). This spectrum is chosen because it has minimal broadening due to electric fields. We subtract κ_{IH} from the extracted linewidth and assume the remaining broadening arises from homogeneous sources (e.g. microwave power broadening); this yields $\kappa_{\text{H}} \approx 1$ MHz. We note that this parameter has only a minor effect on the susceptibility estimates.

Finally, we extract the susceptibility parameters by fitting our model to the empirical values for Π_{\perp} as a function of $\Delta\nu$. In particular, we calculate the least-square error of the data compared to the predicted splittings from our resonant ODMR model, with χ_{\perp}^e and χ_{\parallel}^e as the only free parameters [Fig. S5(a)]^[c]. We find the χ^2 -error is minimized at $\{\chi_{\perp}^e, \chi_{\parallel}^e\} = \{1.43, 0.68\}$ MHz/(V/cm) with a reduced- χ^2 value of $\chi_{\nu}^2 = 0.87$ (with 15 observations and 2 fit parameters). By linearizing our model around the fitted values, we determine the 2σ confidence region of the susceptibility estimates [Fig. S5(b)] and estimate uncertainties of $\sim 5\%$ for χ_{\perp}^e , and $\sim 15\%$ for χ_{\parallel}^e . We also estimate systematic errors by repeating the analysis with the values ρ_c and κ_{IH} indicated in Fig S4(b). This is shown in Fig. S5(b) and leads to a systematic error of $\sim 5\%$ for χ_{\perp}^e , and $\sim 15\%$ for χ_{\parallel}^e . Summing in quadrature, we have a total error estimate of $\sim 7\%$ for χ_{\perp}^e and $\sim 21\%$ for χ_{\parallel}^e .

A few additional remarks are in order. First, we note that our procedure, by focusing on the splitting of the ODMR spectra, depends almost entirely on the magnitude of the most-probable electric field (i.e. E_0) and not on the details of the full distribution (see Section III A). In particular, this is more robust than an analysis that considers the ODMR linewidth, Γ_g , which can depend significantly on the details of the electric-field distribution (Fig S6)^[d]. Second, in principle ρ_c may depend on the temperature, optical excitation frequency, and excitation power, which would invalidate our assumption that ρ_c can be determined from off-resonant room-temperature ODMR [11–13]. However, even if we relax this assumption, the optical transition linewidth provides an additional, independent constraint on the charge-density and susceptibilities. By demanding that $(\rho_c, \chi_{\parallel}^e, \chi_{\perp}^e)$ simultaneously recover $\Pi_{\perp}(\Delta\nu)$ and the excited state linewidth, we find $\rho_c = 15_{-3}^{+7}$, where the super- (sub-) script indicates the upper (lower) bound. The systematic errors on the extracted susceptibilities concordantly increase to $\sim 10\%$ and $\sim 30\%$ for χ_{\perp}^m and χ_{\parallel}^m respectively. Therefore, the essentials of our analysis and conclusions do not depend on an assumption of consistent ρ_c (although our observations support this conclusion for ensemble measurements).

ρ_c to be 15 ± 5 ppm, increasing the systematic errors by a factor of two for both susceptibilities.

As discussed in the main text, one can also derive analytic expressions for the susceptibilities under the approximation that all resonant configurations lie on the highest-probability electric-field sphere intersecting the resonant cone. The derivation amounts to determining the radius of the inscribed sphere as a function of detuning, $E_s(\Delta\nu)$ and then the radius of the circle defined by its intersection with the cone, $E_c(\Delta\nu)$. The location of the elbow in $\Pi_{\perp}(\Delta\nu)$ is given by the detuning $\Delta\nu^*$ such that $E_s(\Delta\nu^*) = E_0$. On the other hand, the slope $\Pi_{\perp}(\Delta\nu)$ is $m_{\Pi} \equiv \frac{dE_c}{d\Delta\nu}$. Let $\alpha \in [0, \pi/2]$ be the exterior angle of the cone (so $\tan(\alpha) = \chi_{\perp}/\chi_{\parallel}$) [Fig. 2(b)]. One finds

$$\sin(\alpha) = m_{\Pi} \cdot \Delta\nu^* / (E_0 \chi_{\perp}^g) \quad (17)$$

$$\frac{\chi_{\parallel}^e}{\chi_{\perp}^g} = \cos(\alpha) \cdot \Delta\nu^* / (E_0 \chi_{\perp}^g). \quad (18)$$

[c] In the vicinity of the positive-contrast peaks, the off-resonant configurations only contribute a flat background, and can hence be neglected in our fitting procedure. This eliminates ϵ_C and off-resonant linewidths as free parameters and thus simplifies the model we use to extract the susceptibilities. To check this approximation, we also extract the susceptibilities using the ϵ_C and off-resonant linewidths extracted from the 5 K spectrum (Table II) and find that they are within statistical error of those determined from our simpler estimation procedure.

[d] In particular, Γ_g is sensitive to the functional form of the tail of the electric field strength distribution. Intuitively, if the electric field distribution decays very slowly, Γ_g will be large since many nearly equal probability electric-field spheres will intersect the resonant cone at different values of E_{\perp} . More formally, the trend that Γ_g increases with $\Delta\nu$ (Fig. S6) indicates the relative decay rate of the electric-field distribution decreases at larger values of E . This is characteristic of a polynomially decaying tail: if $P(E) \sim 1/(E/E_0)^q$ then $\frac{d(\log(P(E)))}{dE} = -q/E$, so the tail decays more slowly at larger E resulting in larger Γ_g . Indeed, it should be possible to quantitatively extract $\frac{d(\log(P(E)))}{dE}$ from $\Gamma_g(\Delta\nu)$ at large $\Delta\nu$, which could yield insight into the underlying short range physics controlling the tail of the electric field distribution.

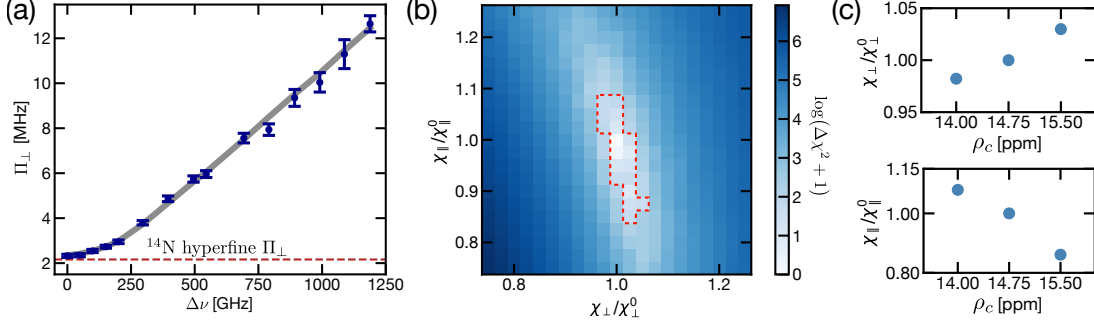


FIG. S5. (a) Experimental Π_{\perp} (dark blue) and model (gray) as functions of $\Delta\nu$. The fit yields $\chi_{\nu}^2 = 0.87$ (b) $\Delta\chi^2$ as a function of χ_{\parallel}^0 and χ_{\perp}^0 . The red-dashed contour denotes the 2σ confidence region. (c) χ_{\perp}^0 and χ_{\parallel}^0 as functions of ρ_c . This quantifies the main source of systematic error in our analysis. Errors are relative to $\{\chi_{\perp}^0, \chi_{\parallel}^0\} = \{1.43, 0.68\}$ MHz/(V/cm)

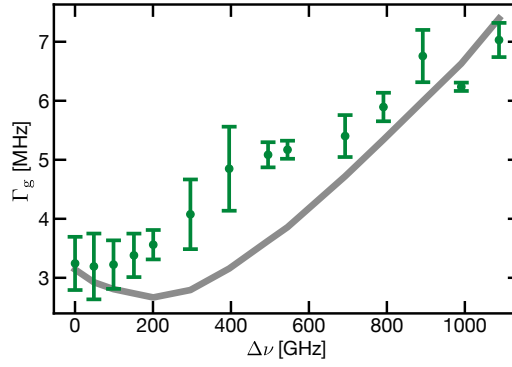


FIG. S6. Resonant ODMR linewidth Γ_g as a function optical detuning. Error bars reflect the difference in the FWHM of Lorentzian fits of the left and right peaks of experimental data. The same analysis applied to the spectra generated by our model yields the gray curve. Although the model accounts for the general trend of increasing Γ at large detuning, there are clear qualitative differences between the experiment and theory. Most notably, the experiment is broader at moderate detunings (200 – 600 GHz) than the model would suggest. This could be because the true electric field distribution decays more slowly than the random charge model predicts (see footnote [d]). The effects of strain may also partially account for the discrepancy.

From these expressions, and setting $\Delta\nu^* = 200$ GHz, $m_{\Pi} = 10^{-5}$ and $E_0\chi_{\perp}^g = 2.4$ MHz, one finds $\chi_{\perp}^e \approx 1.2 \pm 0.2$ MHz/(V/cm) and $\chi_{\parallel}^e \approx 0.8 \pm 0.2$ MHz/(V/cm).^[e] These estimates are within error bars of those derived from our full numerics, indicating the accuracy of this analytic approximation.

V. FITTING TEMPERATURE DEPENDENT SPECTRA

Our procedure for fitting the temperature-dependent ODMR spectra, shown in Fig. 1(a), relies on the same resonant ODMR model, susceptibility parameters, and charge density as in the previous sections. In addition, we find it necessary to vary (i) the ODMR contrast ratio and (ii) broadening parameters at each temperature. Here, we discuss the physical origin of the temperature dependence of these parameters.

Contrast: We attribute the change in contrast to the the fact that increasing temperature broadens the optical transition linewidth, which in turn reduces the density of resonant configurations at a given optical detuning, effectively reducing ϵ_C . Indeed, we find qualitatively that ϵ_C decreases with temperature, though we do not attempt to develop a quantitative model for it.

^[e] The uncertainties are again determined by combining the systematic error in ρ_c (which determines E_0) and a statistical error, which in this case arises from uncertainty in $\Delta\nu^*$ and m_{Π} . The uncertainty in $\Delta\nu^*$ is the dominant statistical error, which we estimate to be 10%

Temp [K]	$\kappa_{\text{H}}^{\text{R}}$ [MHz]	$\kappa_{\text{IH}}^{\text{R}}$ [MHz]	$\kappa_{\text{H}}^{\text{OR}}$ [MHz]	$\kappa_{\text{IH}}^{\text{OR}}$ [MHz]	ϵ_C
5	2.0	4.0	20.0	27.0	10^4
40	2.0	4.0	16.0	16.0	$4 \cdot 10^3$
55	2.0	4.0	12.0	15.0	$1.7 \cdot 10^3$
100	2.0	4.0	9.0	8.0	$1.7 \cdot 10^3$

TABLE II. Summary of parameters used to fit the temperature dependent ODMR spectra [Fig. 1(a)]. The linewidth parameters for resonant configurations are roughly consistent with the more carefully estimated parameters used for susceptibility extraction; the off-resonant linewidth parameters, however, are significantly altered by power-broadening, as we discuss in Section V. In particular, $\kappa_{\text{IH}}^{\text{OR}}$ should not be interpreted as an accurate estimate of the inhomogeneous broadening; instead, we regard it as a phenomenological parameter that controls the amount of broadening which “adds in quadrature” to the electric field [see (6)]. The value of ϵ_C at 5 K is roughly consistent with an estimate based on ϵ_R . Qualitatively, ϵ_C decreases with increasing temperature because the density of resonant states decreases.

Broadening: Experimentally, we observe that off-resonant dips in the ODMR spectrum exhibit larger broadening than the positive-contrast peaks (see Fig. 1(a) in main text). We conjecture two possible causes of this additional broadening. First, there may be different degrees of *light-narrowing* in the resonant and off-resonant configurations. Light-narrowing arises because resonantly driven transitions experience a greater rate of optical pumping than transitions to the phonon-sideband, and hence have a different effective linewidth. In this setting, a greater rate of optical pumping actually *reduces* the effective linewidth [14]. Second, power broadening itself may not be well described by a convolution with a Lorentzian; indeed we find that this is the case even for *off-resonant* ODMR spectra under higher microwave power. Intuitively, large electric fields alter the matrix elements between ground-state sublevels, causing the degree of power-broadening to be electric field strength dependent. To account for this, we treat the off-resonant inhomogeneous broadening parameter, $\kappa_{\text{IH}}^{\text{OR}}$, as a free parameter and find that its best-fit value is comparable to the homogeneous broadening. We emphasize that this is a convenient way to account for the dependence of power broadening on electric field strength and does not constitute a meaningful estimate of the true inhomogeneous broadening due to magnetic fields.

We note that both of these issues are artifacts of working in a microwave power-broadened regime, which is the case for the present temperature-dependent data. For extraction of susceptibilities, ODMR measurements were performed with $100 \times$ lower microwave power, where these effects are suppressed.

VI. SENSITIVITY ESTIMATES

Here, we provide additional details for estimating the sensitivity of our resonant electric-field sensing protocol. The estimates are calibrated based on the sample measured in this work, and then extrapolated to other densities using scaling arguments.

Let us begin by recalling that the sensitivity for an electric-field dependent count rate $R(\delta E)$ is given by

$$\frac{1}{\eta} = \left. \frac{dR}{d(\delta E)} \right|_{\delta E=0} \frac{1}{\sqrt{R(0)}}, \quad (19)$$

$$(20)$$

or equivalently,

$$\frac{1}{\eta} = \left. \frac{d \log(R)}{d(\delta E)} \right|_{\delta E=0} \cdot \sqrt{R(0)}. \quad (21)$$

In our sensing protocol, the fluorescence rate is determined by two effects: (i) the shift of the positive-contrast peaks, and (ii) the change in overall fluorescence. These effects contribute independently to the total signal, such that $R(\delta E) = R_{\text{F}}(\delta E) \cdot R_{\text{II}}(\delta E)$, where R_{F} and R_{II} capture the dependence of fluorescence on optical

detuning and microwave frequency, respectively. The total sensitivity is then

$$\frac{1}{\eta} = \left[\frac{d \log(R_{\Pi})}{d(\delta E)} + \frac{d \log(R_{\text{F}})}{d(\delta E)} \right]_{\delta E=0} \cdot \sqrt{R(0)}, \quad (22)$$

which leads to the equation stated in the main text:

$$\frac{1}{\eta} = \frac{1}{\eta_{\Pi}} + \frac{1}{\eta_{\text{F}}}. \quad (23)$$

For simplicity, we define $R \equiv R(0)$. The sensitivities can be decomposed as

$$\eta_{\Pi} = P_{\Pi} \frac{\Gamma_{\text{g}}}{\chi_{\text{eff}} C_0 C_{\text{r}}} \cdot \frac{1}{\sqrt{R}}, \quad (24)$$

$$\eta_{\text{F}} = P_{\text{F}} \frac{\Gamma_{\text{e}}}{\chi_{\parallel}^{\text{e}} C_{\text{r}}} \cdot \frac{1}{\sqrt{R}}, \quad (25)$$

where Γ (P) is the linewidth (lineshape factor) associated with the ground and excited states, R is the count rate, C_0 is the maximum CW contrast of the resonant ODMR peaks, C_{r} is the ratio of photons resulting from resonant fluorescence to total fluorescence, and $\{\chi_{\text{eff}}, \chi_{\parallel}^{\text{e}}\}$ are the effective ground- and excited-state susceptibilities, respectively.

For our estimates, we assume the ground state ODMR lineshape is Lorentzian, such that $P_{\Pi} \approx 0.77$, and we use the excited-state susceptibility determined in our work: $\chi_{\parallel}^{\text{e}} = 0.7$ MHz/(V/cm); moreover, we determine $\chi_{\text{eff}} \approx 0.41$ and $P_{\text{F}} \approx 0.39$ from our model [Fig. S7(a)] and from experimental data [Fig. S7(b)], respectively. The remaining parameters are discussed below.

A. Parameter calibration

Linewidths: We model the ODMR and optical transition linewidths as containing both an intrinsic broadening and an electric-field induced broadening:

$$\Gamma_{\text{g,e}} = \kappa_{\text{g,e}}^0 + \kappa_{\text{g,e}}^E \bar{\rho}^{2/3}, \quad (26)$$

where $\bar{\rho}$ is a normalized NV density, $\bar{\rho} = \rho_{\text{NV}} / \rho_{\text{NV}}^0$. As discussed in the manuscript, reasonable values for the intrinsic broadening are $\kappa_{\text{g}}^0 \approx 200$ kHz, consistent with observed ODMR linewidths in samples with natural ^{13}C abundance [15, 16], and $\kappa_{\text{e}}^0 \approx 10$ GHz [17, 18]. We calibrate the charge-induced linewidths against our sample ($\rho_{\text{NV}}^0 \approx 8$ ppm), yielding $\kappa_{\text{g}}^E \approx 3.7$ MHz and $\kappa_{\text{e}}^E \approx 10^6$ MHz. We note that here, and throughout our sensitivity estimates, we will assume that the charge environment consists primarily of other uniformly distributed NVs and charge donors, such that $\rho_{\text{c}} = 2\rho_{\text{NV}}$ (see Section III A).

Fluorescence rate: The overall fluorescence rate contains contributions from the resonant and off-resonant configurations. The former is proportional to the density of resonant configurations, and therefore is inversely proportional to the optical transition linewidth. Thus, the fluorescence from resonant configurations R_{R} can be modeled as

$$R_{\text{R}} = r R_0, \quad r = \frac{\kappa^{\text{ref}}}{\kappa_{\text{e}}^0 + \kappa_{\text{e}}^E \bar{\rho}^{2/3}}, \quad (27)$$

where R_0 is the fluorescence rate for a single, off-resonantly driven NV orientation, r is the fluorescence enhancement factor for resonant configurations, and κ^{ref} is a density-independent prefactor. To determine κ^{ref} , we compare the resonant fluorescence at the optimal detuning to the off-resonant fluorescence for detunings far above the ZPL [Fig. S7(b)]. This yields $r \approx 2$, corresponding to $\kappa^{\text{ref}} \approx 2 \cdot 10^6$ MHz; for an optimal sample, we estimate that r can reach $r \approx 100$ at ~ 10 ppb.

To determine the overall count rate, we take into account the fact that our sensing protocol includes signals from one resonant NV orientation and three off-resonant orientations. This is because the bias electric field required to lift the excited-state degeneracy pushes the excited state of three orientations below the excited state of the target orientation, so they are excited by the off-resonant mechanism. In particular, assuming a

Electrometry Method		ρ_{NV} [ppm]	T [K]	Γ [MHz]	P	χ [Hz cm/V]	R [counts/s]	C	η [V/cm $\sqrt{\text{Hz}}$]
Single NV - G.S. [21]		-	$\lesssim 300$	0.05	0.77	17	100	0.3	760
Single NV - E.S. [22]		-	$\lesssim 4$	13	0.77	$7.0 \cdot 10^5$	2500	1	0.29
EIT Ensemble [18]		~ 0.03	$\lesssim 30$	1.0	0.77	9.8	$3.2 \cdot 10^{14}$	0.022	0.20
Off-res. Ensemble [23]		~ 1	$\lesssim 300$	1.0	0.77	17	$5.0 \cdot 10^{14}$	0.02	0.10
Res. Ensemble (Our sample)	F		$\lesssim 200$	10^6	0.39	$7.0 \cdot 10^5$	$2.4 \cdot 10^{15}$	0.54	0.021
	Π_{\perp}	~ 8	$\lesssim 45$	3.9	0.77	6.97	$2.4 \cdot 10^{15}$	0.11	0.077
	Total		$\lesssim 45$	-	-	-	-	-	0.017
Res. Ensemble (Optimal sample)	F		$\lesssim 55$	$2.1 \cdot 10^4$	0.39	$7.0 \cdot 10^5$	$6.9 \cdot 10^{13}$	0.98	0.0014
	Π_{\perp}	~ 0.01	$\lesssim 45$	0.25	0.77	6.97	$6.9 \cdot 10^{13}$	0.21	0.016
	Total		$\lesssim 45$	-	-	-	-	-	0.0013

TABLE III. Summary of NV electrometry protocols and their associated sensitivities, assuming an illumination volume of $\sim 0.1 \text{ mm}^3$ (for ensemble techniques). For our protocol (lower section), we provide both the sensitivity owing to the peak shift (η_{Π}) and the sensitivity owing to the change in overall fluorescence (η_{F}). All sensitivities are given by $\eta = P \frac{\Gamma}{C \chi \sqrt{R}}$, where P is a lineshape dependent prefactor, C is the contrast (i.e. $C = C_0 C_r$ for η_{Π} , and $C = C_r$ for η_{F}), χ is the relevant susceptibility, and Γ is the relevant linewidth (i.e. $\Gamma = \Gamma_{\text{g}}$ for η_{Π} , and $\Gamma = \Gamma_{\text{e}}$ for η_{F}).

(111)-cut diamond, the fluorescence rate due to off-resonant orientations is $R_{\text{OR}} = 5/3 R_0$ [f]. In combination, the total count rate is

$$R = R_0(r + 5/3). \quad (28)$$

We note that R_0 depends on the specific optical setup (e.g. illumination volume, laser power, and collection efficiency). We determine this constant for a similar setup as described in [20] [g]. The final count rate for our sample and for an optimal sample are reported in Table III.

Contrast: We first estimate the maximum CW contrast of the positive-contrast peaks, $C_0 \approx 0.21$, from the experimental data [Fig. S7(c)] [h]. However, of the total counts, only the resonant fraction, C_r , contributes to sensing. Therefore, the actual contrast of the resonant ODMR peaks is $C = C_0 C_r$; meanwhile, for sensing via direct variation in fluorescence (η_{F}), the relevant contrast is C_r . For a (111)-cut sample, we have

$$C_r = \frac{r}{(r + 5/3)}, \quad (29)$$

where r is the resonant enhancement factor defined in (27).

Bias electric field: In addition to the sensitivity estimates provided in the manuscript, we estimate the bias field required to spectrally isolate the crystallographic orientation used in our sensing protocol [Fig. S7(d)]. Given a bias field parallel to one of the NV groups, three other groups will actually be shifted by the electric field *below* the target group since $\chi_{\perp}^{\text{e}} \approx 2\chi_{\parallel}^{\text{e}}$. Therefore, we determine this bias field by demanding the lowest-energy NV group parallel to the bias field is at least $\Gamma_{\text{e}}/2$ above the lowest three NV groups.

[f] The factor of 5/3 arises because the three off-resonant groups are not perpendicular to the laser polarization [19].

[g] In particular, we rescale their reported count rate by the ratio of our sample's NV density to their sample's density and correct for a difference in laser polarization. We also divide by 8, since only one NV crystallographic orientation will be used in the sensing protocol.

[h] In particular, for a (111)-cut diamond, $C_0 = 8/3 C_{\text{exp}}$, where C_{exp} is the experimentally observed contrast.

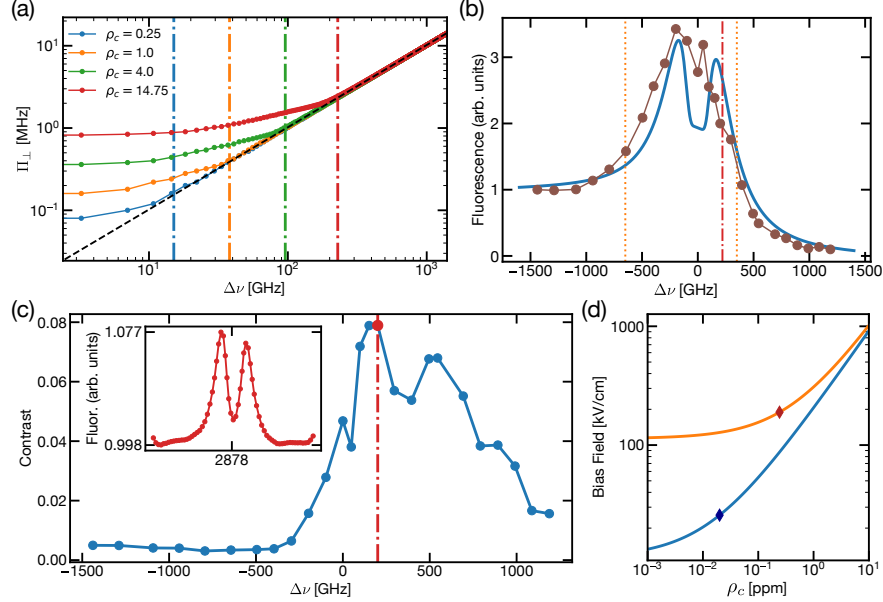


FIG. S7. (a) Π_{\perp} as a function of $\Delta\nu$ for various ρ_c . Dash-dot vertical lines indicate the optimal operating $\Delta\nu$ for our sensing proposal. In particular, we choose the smallest $\Delta\nu$ for which Π_{\perp} depends linearly on $\Delta\nu$. This maximizes χ_{eff} and the resonant fluorescence. (b) Fluorescence as a function of $\Delta\nu$ from experiment (brown) and theory (solid blue). The dash-dot vertical line indicates the optimal operating $\Delta\nu$ for our sample. We estimate $\Gamma_e \approx 1$ THz, ignoring asymmetry (dashed orange lines). (c) Contrast of resonant ODMR (with a 20 G applied magnetic field perpendicular to the NV axis) as a function of $\Delta\nu$. The red marker and dash-dot line indicates the contrast at the optimal operating detuning. Since magnetically split groups provide additional background for the central peak, the maximum CW ODMR contrast C_0 is a factor 8/3 larger than what is observed (see Section VI A) [19]. (inset) Experimental resonant ODMR at the optimal operating $\Delta\nu$. (d) Electric field bias required for our sensing procedure as a function of ρ_c assuming $\kappa_e^0 = 10$ GHz (blue) and $\kappa_e^0 = 100$ GHz (orange). The blue and red diamonds mark the bias field required at optimal NV densities.

B. Scaling with density

Here, we determine how sensitivity degrades in the high-density regime. We consider an ideal limit for which there is minimal charge broadening, i.e. $\rho \equiv \rho_c = 2\rho_{\text{NV}}$ and no density-dependent broadening other than internal electric-fields. As discussed above, in the charge-dominated regime the ODMR and optical transition linewidths (Γ_g, Γ_e) are proportional to the average electric field strength, which scales as $\rho_{\text{NV}}^{2/3}$. In this regime, we also have $r \propto \rho^{-2/3}$ and $r \ll 5/3$, implying $C_r \propto \rho^{-2/3}$ and $R \sim \rho$. Thus the sensitivity scaling at high-densities is given by

$$\eta \propto \frac{\Gamma}{C_r \sqrt{R}} \propto \frac{\rho^{2/3}}{\rho^{-2/3} \sqrt{\rho}} = \rho^{5/6} \quad (30)$$

as stated in the main text (Fig. 3). The scaling for typical electrometry protocols may be similarly determined. In this case, all photons are scattered off-resonantly and C_r is no longer relevant in the sensitivity expressions. Then

$$\eta \sim \frac{\rho^{2/3}}{\sqrt{\rho}} = \rho^{1/6} \quad (31)$$

as shown in Fig. 3 of the main text.

	χ_{\perp} [Hz/(V/cm)]	χ_{\parallel} [Hz/(V/cm)]
E.S. - measured (our work)	$1.4 \pm 0.1 (\times 10^6)$	$0.7 \pm 0.1 (\times 10^6)$
E.S. - electronic effect	$1.6 (\times 10^6)$	$0.6 (\times 10^6)$
G.S. - measured [1]	17 ± 2.5	0.35 ± 0.02
G.S. - spin-spin effect	76	0

TABLE IV. Comparison between measured susceptibilities and theoretical estimates. Details of the theoretical estimates are provided in this work and accompanying references.

C. Insensitivity to perpendicular fields

Our sensing protocol enables the detection of small variations in the electric field *parallel* to a particular NV axis. One might be concerned that additional sensitivity to fields *perpendicular* to the axis could lead to ambiguity in determining the direction of the detected field. Fortunately, this issue is avoided by the fact that the sensitivity to external perpendicular fields is suppressed by the random orientation of internal electric fields.

To see this, consider the level shift induced by a small perpendicular field δE_{\perp} oriented in the \hat{x} direction. Assume that internal perpendicular fields have strength E_0 and are randomly oriented in the xy plane. The ensemble-average level shift, $\delta\nu$, of the lower branch is then approximated by

$$\delta\nu/\chi_{\perp}^e \approx \frac{1}{2\pi} \int d\theta \sqrt{E_0^2 + \delta E_{\perp}^2 + 2\delta E_{\perp} E_0 \cos\theta} - E_0 \quad (32)$$

$$\approx \frac{1}{2\pi} \int d\theta \cos\theta \delta E_{\perp} + O(\delta E_{\perp}^2/E_0) \quad (33)$$

$$\approx O(\delta E_{\perp}^2/E_0). \quad (34)$$

That is, since θ is uniformly distributed (a consequence of the spherical symmetry of the electric-field distribution), the ensemble shift vanishes to leading order. Intuitively, for every NV for which the perturbation constructively adds to the already-present perpendicular field, there is another NV for which these fields interfere. The net effect on the ensemble is thus suppressed.

VII. THEORETICAL ESTIMATES OF SUSCEPTIBILITIES

In this section, we discuss the physical origin of the NV's electric field susceptibility in both the ground and excited state, and compare the measured susceptibility parameters to theoretical estimates (Table IV).

A. Excited state

While it is well understood that the orbital doublet nature of the excited state allows for a linear Stark shift, the microscopic origin of this shift can in principle be explained by two different mechanisms [8]. One mechanism, the electronic effect, is based on the polarization of the NV's electronic wavefunction. The second mechanism, the ionic effect, consists of the relative displacement of the ions and is thus closely related to piezoelectricity. The two effects are indistinguishable from a group theoretic perspective and, in general, both will contribute to the total susceptibility. Below we estimate the susceptibilities based on the electronic effect and find good agreement with the measured values (Table IV). On the other hand, the ionic effect was previously estimated with *ab initio* simulations and was found to be on the same order of magnitude [8]. Thus, a more precise calculation of the excited susceptibilities should take into account both effects.

To estimate the electronic effect, we consider the molecular model of the defect center, in which the NV's single-particle orbitals are constructed from non-overlapping atomic orbitals, $\{\sigma_1, \sigma_2, \sigma_3, \sigma_N\}$, centered on the three carbon ions and the nitrogen ion, respectively [8, 9]. In particular, the single-particle orbitals are

given by

$$e_x = \frac{1}{\sqrt{6}} (2\sigma_1 - \sigma_2 - \sigma_3) \quad (35)$$

$$e_y = \frac{1}{\sqrt{2}} (\sigma_2 - \sigma_3) \quad (36)$$

$$a_1 = \frac{1}{\sqrt{3 + \lambda^2}} (\sigma_1 + \sigma_2 + \sigma_3 + \lambda\sigma_N) , \quad (37)$$

where σ_1 is the carbon orbital that lies in the xy plane, and $\lambda \approx 0.7$ is determined from density functional theory (DFT) calculations [24]^[i] These orbitals are combined to form the 3A_2 ground state

$$|A_2\rangle = \frac{1}{\sqrt{2}} (|e_x e_y\rangle - |e_y e_x\rangle) \quad (38)$$

and the two 3E excited states

$$|X\rangle = \frac{1}{\sqrt{2}} (|a_1 e_x\rangle - |e_x a_1\rangle) \quad (39)$$

$$|Y\rangle = \frac{1}{\sqrt{2}} (|a_1 e_y\rangle - |e_y a_1\rangle) . \quad (40)$$

From first-order perturbation theory, the electric field susceptibility is determined by the permanent dipole of the excited state. For the transverse susceptibility, it is sufficient to calculate the dipole moment along the x -axis, which is diagonal in the $\{|X\rangle, |Y\rangle\}$ basis:

$$d_\perp = -e \langle X | x_1 + x_2 | X \rangle , \quad (41)$$

where $x_{1,2}$ are the single particle positions and e is the elementary charge. In the single-particle basis, this reduces to

$$|d_\perp| = e \langle e_x | x | e_x \rangle \quad (42)$$

$$\approx \frac{e}{2} \langle \sigma_1 | x | \sigma_1 \rangle , \quad (43)$$

where we have approximated the full integral by assuming non-overlapping atomic orbitals. For the longitudinal direction, the relevant term is the relative dipole moment between between the ground and excited state. This is given by

$$d_\parallel = -e [\langle X | z_1 + z_2 | X \rangle - \langle A_2 | z_1 + z_2 | A_2 \rangle] \quad (44)$$

$$= -e [\langle a_1 | z | a_1 \rangle - \langle e_x | z | e_x \rangle] \quad (45)$$

$$\approx \frac{e\lambda^2}{3 + \lambda^2} [\langle \sigma_1 | z | \sigma_1 \rangle - \langle \sigma_N | z | \sigma_N \rangle] . \quad (46)$$

Inserting orbital expectation values from DFT calculations, we obtain $|d_\perp| \approx e(0.67 \text{ \AA})$ and $d_\parallel \approx e(0.26 \text{ \AA})$ [24, 25]. This yields susceptibility estimates of $\{\chi_\perp^e, \chi_\parallel^e\} = \{1.6, 0.6\} \text{ MHz}/(\text{V}/\text{cm})$, in good agreement with the values measured in this work (Table IV).

B. Ground state

The ground state of the NV center is an orbital singlet, leading to the naive expectation that a linear Stark effect is disallowed. This, however, contradicts experimental observation of $\{\chi_\perp^g, \chi_\parallel^g\} = \{17, 0.35\} \text{ Hz}/(\text{V}/\text{cm})$

^[i] We note that there is a fourth state with the same symmetry properties as a_1 (i.e. transforms according to the totally symmetric A_1 irreducible representation), but it is higher in energy than the other three and therefore not relevant for this discussion [8].

[1]. The conventional explanation is that the ground state inherits a permanent dipole moment from the excited state due to spin-orbit coupling [26, 27]. While such coupling is indeed present, its magnitude is likely insufficient to account for the measured transverse field susceptibility. More recently, it was suggested that the ground state transverse susceptibility arises from the interplay between electric fields and the dipolar spin-spin interaction [27]. In particular, the effect is as follows: At first order in perturbation theory, the ground state wavefunction is mixed with the excited state by the presence of an electric field; this perturbation then couples to the ground-state spin degrees of freedom via the dipolar spin-spin interaction. Below we estimate the magnitude of the effect (which was not reported in [27]) and find good agreement with the known ground state transverse susceptibility (Table IV). We also hasten to emphasize that this effect only occurs to leading order for transverse electric fields, which naturally explains the 50-fold anisotropy between χ_{\perp}^{g} and $\chi_{\parallel}^{\text{g}}$.

As in the case of the excited state, it is sufficient to consider the transverse susceptibility for a field along the x -axis. At first order in perturbation theory, an electric field $\vec{E} = E_{\perp} \hat{x}$ mixes the ground state $|A_2\rangle$ with the excited state $|Y\rangle$:

$$|A_2'\rangle = |A_2\rangle + \frac{E_{\perp}}{\nu_0} d'_{\perp} |Y\rangle, \quad (47)$$

where e is the elementary charge, and $\nu_0 \approx 1.9$ eV is the energy splitting between the ground and excited state. d'_{\perp} is the dipole moment associated with the transition between the states,

$$d'_{\perp} = -e \langle A_2 | x_1 + x_2 | X \rangle. \quad (48)$$

In the single-particle basis, this becomes

$$|d'_{\perp}| = e \langle e_x | x | a_1 \rangle \quad (49)$$

$$\approx \frac{3e}{\sqrt{6(3 + \lambda^2)}} \langle \sigma_1 | x | \sigma_1 \rangle. \quad (50)$$

Based on DFT results, we estimate $|d'_{\perp}| \approx e(0.88 \text{ \AA})$ [24, 27].

To determine the effect on the ground-state spin degrees of freedom, it is then necessary to consider the dipolar spin-spin interaction, given by

$$H_{ss} = \frac{\mu_0 \mu_B^2 g^2}{8\pi h} \frac{3(\mathbf{S} \cdot \hat{r}_{12})(\mathbf{S} \cdot \hat{r}_{12}) - \mathbf{S} \cdot \mathbf{S}}{r_{12}^3}, \quad (51)$$

where μ_B is the Bohr magneton, $g_e \approx 2$ is the NV gyromagnetic ratio, \mathbf{S} are spin-1 operators, and \vec{r}_{12} is the relative displacement between the two particles. In the absence of an external perturbation, the orbital degrees of freedom are integrated with respect to the ground-state wavefunction $|A_2\rangle$, and the only non-vanishing term is the ground-state splitting, $H_{ss}^0 = \Delta_{\text{ZFS}} S_z^2$. For the perturbed wavefunction $|A_2'\rangle$, there is an additional non-vanishing term, corresponding to a ground-state Stark shift:

$$H'_{ss} = \Delta_{\text{ZFS}} S_z^2 + \Pi_{\perp} (S_y^2 - S_x^2). \quad (52)$$

The magnitude of Π_{\perp} is given by

$$\Pi_{\perp} = 2 \frac{E_{\perp}}{\nu_0} |d'_{\perp}| D_E \quad (53)$$

with

$$D_E = \frac{3\mu_0 \mu_B^2 g_e^2}{8\pi h} \langle A_2 | \frac{x_{12}^2 - y_{12}^2}{r_{12}^5} | Y \rangle \quad (54)$$

$$= \frac{3\mu_0 \mu_B^2 g_e^2}{8\pi h} \langle a_1 e_y | \frac{x_{12}^2 - y_{12}^2}{r_{12}^5} (|e_x e_y\rangle - |e_y e_x\rangle). \quad (55)$$

Assuming non-overlapping orbitals, this simplifies to

$$D_E \approx \frac{3\mu_0 \mu_B^2 g_e^2}{8\pi h} \frac{2}{\sqrt{6(3 + \lambda^2)}} \left(\langle \sigma_1 \sigma_2 | \frac{x_{12}^2 - y_{12}^2}{r_{12}^5} | \sigma_1 \sigma_2 \rangle + \langle \sigma_2 \sigma_3 | \frac{x_{12}^2 - y_{12}^2}{r_{12}^5} | \sigma_2 \sigma_3 \rangle \right). \quad (56)$$

We further approximate the two-particle integrals with the semiclassical position of each particle individually [25, 27]:

$$\langle \sigma_1 \sigma_2 | \frac{x_{12}^2 - y_{12}^2}{r_{12}^5} | \sigma_1 \sigma_2 \rangle \approx \frac{(\langle x \rangle_1 - \langle x \rangle_2)^2 - (\langle y \rangle_1 - \langle y \rangle_2)^2}{(\langle r \rangle_1 - \langle r \rangle_2)^5} = \frac{1}{2(\langle r \rangle_1 - \langle r \rangle_2)^3} = \frac{1}{6\sqrt{3}\langle x \rangle_1^3} \quad (57)$$

$$\langle \sigma_2 \sigma_3 | \frac{x_{12}^2 - y_{12}^2}{r_{12}^5} | \sigma_2 \sigma_3 \rangle \approx \frac{(\langle x \rangle_2 - \langle x \rangle_3)^2 - (\langle y \rangle_2 - \langle y \rangle_3)^2}{(\langle r \rangle_2 - \langle r \rangle_3)^5} = \frac{1}{(\langle r \rangle_1 - \langle r \rangle_2)^3} = \frac{1}{3\sqrt{3}\langle x \rangle_1^3}, \quad (58)$$

where $\langle \cdot \rangle_i = \langle \sigma_i | \cdot | \sigma_i \rangle$ and in the final expressions we utilized the triangular symmetry of the carbon orbitals. This leads to

$$D_E \approx \frac{\mu_0 \mu_B^2 g_e^2}{8\pi h \sqrt{2(3 + \lambda^2)}} \frac{1}{\langle x \rangle_1^3}. \quad (59)$$

Altogether, this predicts a susceptibility of $\chi_{\perp}^e \approx 76 \text{ Hz}/(\text{V}/\text{cm})$, which is within a factor of 5 of the measured value.

Crucially, the spin-spin effect also provides a group theoretic explanation for the large anisotropy between the ground state transverse and longitudinal susceptibilities. In particular, the longitudinal dipole moment between the ground and excited states,

$$d'_{\parallel} = -e \langle A_2 | z_1 + z_2 | X \rangle, \quad (60)$$

vanishes due to symmetry, implying that *only* a transverse electric field can mix the ground and excited states to leading order. We thus postulate that the relatively strong transverse susceptibility arises from the proposed spin-spin effect, while the weak longitudinal effect arises from entirely different physical origin, e.g. based on spin-orbit coupling or the ionic (piezoelectric) effect.

-
- [1] E. Van Oort and M. Glasbeek, *Chemical Physics Letters* **168**, 529 (1990).
 - [2] V. M. Acosta, E. Bauch, M. P. Ledbetter, C. Santori, K.-M. C. Fu, P. E. Barclay, R. G. Beausoleil, H. Linget, J. F. Roch, F. Treussart, S. Chemerisov, W. Gawlik, and D. Budker, *Phys. Rev. B* **80**, 115202 (2009).
 - [3] R. Akhmedzhanov, L. Gushchin, N. Nizov, V. Nizov, D. Sobgayda, I. Zelensky, and P. Hemmer, *Physical Review A* **94**, 063859 (2016).
 - [4] M. L. Goldman, M. W. Doherty, A. Sipahigil, N. Y. Yao, S. D. Bennett, N. B. Manson, A. Kubanek, and M. D. Lukin, *Physical Review B* **91**, 165201 (2015).
 - [5] K.-M. C. Fu, C. Santori, P. E. Barclay, L. J. Rogers, N. B. Manson, and R. G. Beausoleil, *Physical Review Letters* **103**, 256404 (2009).
 - [6] T. Mittiga, S. Hsieh, C. Zu, B. Kobrin, F. Machado, P. Bhattacharyya, N. Rui, A. Jarmola, S. Choi, D. Budker, *et al.*, *Physical review letters* **121**, 246402 (2018).
 - [7] S. Bhagavantam and D. a. a. S. N. Rao, *Nature* **161**, 729 (1948), number: 4097 Publisher: Nature Publishing Group.
 - [8] J. R. Maze, A. Gali, E. Togan, Y. Chu, A. Trifonov, E. Kaxiras, and M. D. Lukin, *New Journal of Physics* **13**, 025025 (2011).
 - [9] M. W. Doherty, N. B. Manson, P. Delaney, and L. C. L. Hollenberg, *New Journal of Physics* **13**, 025019 (2011).
 - [10] L. Robledo, L. Childress, H. Bernien, B. Hensen, P. F. A. Alkemade, and R. Hanson, *Nature* **477**, 574 (2011), number: 7366, Publisher: Nature Publishing Group.
 - [11] L. C. Bassett, F. J. Heremans, C. G. Yale, B. B. Buckley, and D. D. Awschalom, *Phys. Rev. Lett.* **107**, 266403 (2011).
 - [12] V. M. Acosta, C. Santori, A. Faraon, Z. Huang, K.-M. C. Fu, A. Stacey, D. A. Simpson, K. Ganesan, S. Tomljenovic-Hanic, A. D. Greentree, S. Prawer, and R. G. Beausoleil, *Physical Review Letters* **108**, 206401 (2012).
 - [13] N. B. Manson, M. Hedges, M. S. J. Barson, R. Ahlefeldt, M. W. Doherty, H. Abe, T. Ohshima, and M. J. Sellars, *New Journal of Physics* **20**, 113037 (2018).
 - [14] K. Jensen, V. M. Acosta, A. Jarmola, and D. Budker, *Physical Review B* **87**, 014115 (2013).
 - [15] L. Pham, *Magnetic Field Sensing with Nitrogen-Vacancy Color Centers in Diamond*, Ph.D. thesis, Harvard University (2013).
 - [16] G. Balasubramanian, P. Neumann, D. Twitchen, M. Markham, R. Kolesov, N. Mizuochi, J. Isoya, J. Achard, J. Beck, J. Tissler, V. Jacques, P. R. Hemmer, F. Jelezko, and J. Wrachtrup, *Nature Materials* **8**, 383 (2009).

- [17] A. Batalov, C. Zierl, T. Gaebel, P. Neumann, I.-Y. Chan, G. Balasubramanian, P. R. Hemmer, F. Jelezko, and J. Wrachtrup, *Physical Review Letters* **100**, 077401 (2008).
- [18] V. M. Acosta, K. Jensen, C. Santori, D. Budker, and R. G. Beausoleil, *Phys. Rev. Lett.* **110**, 213605 (2013).
- [19] M. S. J. Barson, P. Peddibhotla, P. Ovarthaiyapong, K. Ganesan, R. L. Taylor, M. Gebert, Z. Mielens, B. Koslowski, D. A. Simpson, L. P. McGuinness, J. McCallum, S. Prawer, S. Onoda, T. Ohshima, A. C. Bleszynski Jayich, F. Jelezko, N. B. Manson, and M. W. Doherty, *Nano Letters* **17**, 1496 (2017), publisher: American Chemical Society.
- [20] E. H. Chen, H. A. Clevenson, K. A. Johnson, L. M. Pham, D. R. Englund, P. R. Hemmer, and D. A. Braje, *Physical Review A* **95**, 053417 (2017).
- [21] F. Dolde, H. Fedder, M. W. Doherty, T. Nöbauer, F. Rempp, G. Balasubramanian, T. Wolf, F. Reinhard, L. C. Hollenberg, F. Jelezko, *et al.*, *Nature Physics* **7**, 459 (2011).
- [22] Y. Chu, *Quantum optics with atom-like systems in diamond*, Ph.D. thesis, Harvard University (2014).
- [23] J. Michl, J. Steiner, A. Denisenko, A. Blau, A. Zimmermann, K. Nakamura, H. Sumiya, S. Onoda, P. Neumann, J. Isoya, and J. Wrachtrup, *Nano Letters* **19**, 4904 (2019).
- [24] A. Gali, M. Fyta, and E. Kaxiras, *Physical Review B* **77**, 155206 (2008).
- [25] M. W. Doherty, V. V. Struzhkin, D. A. Simpson, L. P. McGuinness, Y. Meng, A. Stacey, T. J. Karle, R. J. Hemley, N. B. Manson, L. C. Hollenberg, and S. Prawer, *Physical Review Letters* **112**, 047601 (2014).
- [26] F. Dolde, H. Fedder, M. W. Doherty, T. Nöbauer, F. Rempp, G. Balasubramanian, T. Wolf, F. Reinhard, L. C. L. Hollenberg, F. Jelezko, and J. Wrachtrup, *Nature Physics* **7**, 459 (2011).
- [27] M. W. Doherty, J. Michl, F. Dolde, I. Jakobi, P. Neumann, N. B. Manson, and J. Wrachtrup, *New Journal of Physics* **16**, 063067 (2014).